# Dalitz plot analyses of $J/\psi \to \pi^+\pi^-\pi^0$, $J/\psi \to K^+K^-\pi^0$, and $J/\psi \to K_s^0 K^\pm \pi^\mp$ produced via $e^+e^-$ annihilation with initial-state radiation

J. P. Lees,[1] V. Poireau,[1] V. Tisserand,[1] E. Grauges,[2] A. Palano,[3,†] G. Eigen,[4] D. N. Brown,[5] Yu. G. Kolomensky,[5] M. Fritsch,[6] H. Koch,[6] T. Schroeder,[6] C. Hearty,[7a,7b] T. S. Mattison,[7b] J. A. McKenna,[7b] R. Y. So,[7b] V. E. Blinov,[8a,8b,8c] A. R. Buzykaev,[8a] V. P. Druzhinin,[8a,8b] V. B. Golubev,[8a,8b] E. A. Kravchenko,[8a,8b] A. P. Onuchin,[8a,8b,8c] S. I. Serednyakov,[8a,8b] Yu. I. Skovpen,[8a,8b] E. P. Solodov,[8a,8b] K. Yu. Todyshev,[8a,8b] A. J. Lankford,[9] J. W. Gary,[10] O. Long,[10] A. M. Eisner,[11] W. S. Lockman,[11] W. Panduro Vazquez,[11] D. S. Chao,[12] C. H. Cheng,[12] B. Echenard,[12] K. T. Flood,[12] D. G. Hitlin,[12] J. Kim,[12] T. S. Miyashita,[12] P. Ongmongkolkul,[12] F. C. Porter,[12] M. Röhrken,[12] Z. Huard,[13] B. T. Meadows,[13] B. G. Pushpawela,[13] M. D. Sokoloff,[13] L. Sun,[13,‡] J. G. Smith,[14] S. R. Wagner,[14] D. Bernard,[15] M. Verderi,[15] D. Bettoni,[16a] C. Bozzi,[16a] R. Calabrese,[16a,16b] G. Cibinetto,[16a,16b] E. Fioravanti,[16a,16b] I. Garzia,[16a,16b] E. Luppi,[16a,16b] V. Santoro,[16a] A. Calcaterra,[17] R. de Sangro,[17] G. Finocchiaro,[17] S. Martellotti,[17] P. Patteri,[17] I. M. Peruzzi,[17] M. Piccolo,[17] M. Rotondo,[17] A. Zallo,[17] S. Passaggio,[18] C. Patrignani,[18,§] H. M. Lacker,[19] B. Bhuyan,[20] A. P. Szczepaniak,[21,†] U. Mallik,[22] C. Chen,[23] J. Cochran,[23] S. Prell,[23] H. Ahmed,[24] M. R. Pennington,[25] A. V. Gritsan,[26] N. Arnaud,[27] M. Davier,[27] F. Le Diberder,[27] A. M. Lutz,[27] G. Wormser,[27] D. J. Lange,[28] D. M. Wright,[28] J. P. Coleman,[29] E. Gabathuler,[29,*] D. E. Hutchcroft,[29] D. J. Payne,[29] C. Touramanis,[29] A. J. Bevan,[30] F. Di Lodovico,[30] R. Sacco,[30] G. Cowan,[31] Sw. Banerjee,[32] D. N. Brown,[32] C. L. Davis,[32] A. G. Denig,[33] W. Gradl,[33] K. Griessinger,[33] A. Hafner,[33] K. R. Schubert,[33] R. J. Barlow,[34,∥] G. D. Lafferty,[34] R. Cenci,[35] A. Jawahery,[35] D. A. Roberts,[35] R. Cowan,[36] S. H. Robertson,[37] B. Dey,[38a] N. Neri,[38a] F. Palombo,[38a,38b] R. Cheaib,[39] L. Cremaldi,[39] R. Godang,[39,**] D. J. Summers,[39] P. Taras,[40] G. De Nardo,[41] C. Sciacca,[41] G. Raven,[42] C. P. Jessop,[43] J. M. LoSecco,[43] K. Honscheid,[44] R. Kass,[44] A. Gaz,[45a] M. Margoni,[45a,45b] M. Posocco,[45a] G. Simi,[45a,45b] F. Simonetto,[45a,45b] R. Stroili,[45a,45b] S. Akar,[46] E. Ben-Haim,[46] M. Bomben,[46] G. R. Bonneaud,[46] G. Calderini,[46] J. Chauveau,[46] G. Marchiori,[46] J. Ocariz,[46] M. Biasini,[47a,47b] E. Manoni,[47a] A. Rossi,[47a] G. Batignani,[48a,48b] S. Bettarini,[48a,48b] M. Carpinelli,[48a,48b,††] G. Casarosa,[48a,48b] M. Chrzaszcz,[48a] F. Forti,[48a,48b] M. A. Giorgi,[48a,48b] A. Lusiani,[48a,48c] B. Oberhof,[48a,48b] E. Paoloni,[48a,48b] M. Rama,[48a] G. Rizzo,[48a,48b] J. J. Walsh,[48a] A. J. S. Smith,[49] F. Anulli,[50a] R. Faccini,[50a,50b] F. Ferrarotto,[50a] F. Ferroni,[50a,50b] A. Pilloni,[50a,50b] G. Piredda,[50a,*] C. Bünger,[51] S. Dittrich,[51] O. Grünberg,[51] M. Heß,[51] T. Leddig,[51] C. Voß,[51] R. Waldi,[51] T. Adye,[52] F. F. Wilson,[52] S. Emery,[53] G. Vasseur,[53] D. Aston,[54] C. Cartaro,[54] M. R. Convery,[54] J. Dorfan,[54] W. Dunwoodie,[54] M. Ebert,[54] R. C. Field,[54] B. G. Fulsom,[54] M. T. Graham,[54] C. Hast,[54] W. R. Innes,[54] P. Kim,[54] D. W. G. S. Leith,[54] S. Luitz,[54] D. B. MacFarlane,[54] D. R. Muller,[54] H. Neal,[54] B. N. Ratcliff,[54] A. Roodman,[54] M. K. Sullivan,[54] J. Va'vra,[54] W. J. Wisniewski,[54] M. V. Purohit,[55] J. R. Wilson,[55] A. Randle-Conde,[56] S. J. Sekula,[56] M. Bellis,[57] P. R. Burchat,[57] E. M. Puccio,[57] M. S. Alam,[58] J. A. Ernst,[58] R. Gorodeisky,[59] N. Guttman,[59] D. R. Peimer,[59] A. Soffer,[59] S. M. Spanier,[60] J. L. Ritchie,[61] R. F. Schwitters,[61] J. M. Izen,[62] X. C. Lou,[62] F. Bianchi,[63a,63b] F. De Mori,[63a,63b] A. Filippi,[63a] D. Gamba,[63a,63b] L. Lanceri,[64] L. Vitale,[64] F. Martinez-Vidal,[65] A. Oyanguren,[65] J. Albert,[66b] A. Beaulieu,[66b] F. U. Bernlochner,[66b] G. J. King,[66b] R. Kowalewski,[66b] T. Lueck,[66b] I. M. Nugent,[66b] J. M. Roney,[66b] R. J. Sobie,[66a,66b] N. Tasneem,[66b] T. J. Gershon,[67] P. F. Harrison,[67] T. E. Latham,[67] R. Prepost,[68] and S. L. Wu[68]

(*BABAR* Collaboration)

[1]*Laboratoire d'Annecy-le-Vieux de Physique des Particules (LAPP), Université de Savoie, CNRS/IN2P3, F-74941 Annecy-Le-Vieux, France*
[2]*Universitat de Barcelona, Facultat de Fisica, Departament ECM, E-08028 Barcelona, Spain*
[3]*INFN Sezione di Bari and Dipartimento di Fisica, Università di Bari, I-70126 Bari, Italy*
[4]*University of Bergen, Institute of Physics, N-5007 Bergen, Norway*
[5]*Lawrence Berkeley National Laboratory and University of California, Berkeley, California 94720, USA*
[6]*Ruhr Universität Bochum, Institut für Experimentalphysik 1, D-44780 Bochum, Germany*
[7a]*Institute of Particle Physics, Vancouver, British Columbia, Canada V6T 1Z1*
[7b]*University of British Columbia, Vancouver, British Columbia, Canada V6T 1Z1*
[8a]*Budker Institute of Nuclear Physics SB RAS, Novosibirsk 630090, Russia*
[8b]*Novosibirsk State University, Novosibirsk 630090, Russia*
[8c]*Novosibirsk State Technical University, Novosibirsk 630092, Russia*
[9]*University of California at Irvine, Irvine, California 92697, USA*
[10]*University of California at Riverside, Riverside, California 92521, USA*
[11]*University of California at Santa Cruz, Institute for Particle Physics, Santa Cruz, California 95064, USA*
[12]*California Institute of Technology, Pasadena, California 91125, USA*
[13]*University of Cincinnati, Cincinnati, Ohio 45221, USA*
[14]*University of Colorado, Boulder, Colorado 80309, USA*
[15]*Laboratoire Leprince-Ringuet, Ecole Polytechnique, CNRS/IN2P3, F-91128 Palaiseau, France*

[16a] *INFN Sezione di Ferrara, I-44122 Ferrara, Italy*

[16b] *Dipartimento di Fisica e Scienze della Terra, Università di Ferrara, I-44122 Ferrara, Italy*

[17] *INFN Laboratori Nazionali di Frascati, I-00044 Frascati, Italy*

[18] *INFN Sezione di Genova, I-16146 Genova, Italy*

[19] *Humboldt-Universität zu Berlin, Institut für Physik, D-12489 Berlin, Germany*

[20] *Indian Institute of Technology Guwahati, Guwahati, Assam 781 039, India*

[21] *Indiana University, Bloomington, Indiana 47405, USA*

[22] *University of Iowa, Iowa City, Iowa 52242, USA*

[23] *Iowa State University, Ames, Iowa 50011, USA*

[24] *Physics Department, Jazan University, Jazan 22822, Kingdom of Saudi Arabia*

[25] *Thomas Jefferson National Accelerator Facility, Newport News, Virginia 23606, USA*

[26] *Johns Hopkins University, Baltimore, Maryland 21218, USA*

[27] *Laboratoire de l'Accélérateur Linéaire, IN2P3/CNRS et Université Paris-Sud 11,*
*Centre Scientifique d'Orsay, F-91898 Orsay Cedex, France*

[28] *Lawrence Livermore National Laboratory, Livermore, California 94550, USA*

[29] *University of Liverpool, Liverpool L69 7ZE, United Kingdom*

[30] *Queen Mary, University of London, London E1 4NS, United Kingdom*

[31] *University of London, Royal Holloway and Bedford New College, Egham,*
*Surrey TW20 0EX, United Kingdom*

[32] *University of Louisville, Louisville, Kentucky 40292, USA*

[33] *Johannes Gutenberg-Universität Mainz, Institut für Kernphysik, D-55099 Mainz, Germany*

[34] *University of Manchester, Manchester M13 9PL, United Kingdom*

[35] *University of Maryland, College Park, Maryland 20742, USA*

[36] *Massachusetts Institute of Technology, Laboratory for Nuclear Science,*
*Cambridge, Massachusetts 02139, USA*

[37] *Institute of Particle Physics and McGill University, Montréal, Québec, Canada H3A 2T8*

[38a] *INFN Sezione di Milano, I-20133 Milano, Italy*

[38b] *Dipartimento di Fisica, Università di Milano, I-20133 Milano, Italy*

[39] *University of Mississippi, University, Mississippi 38677, USA*

[40] *Université de Montréal, Physique des Particules, Montréal, Québec, Canada H3C 3J7*

[41] *INFN Sezione di Napoli and Dipartimento di Scienze Fisiche, Università di Napoli Federico II,*
*I-80126 Napoli, Italy*

[42] *NIKHEF, National Institute for Nuclear Physics and High Energy Physics,*
*NL-1009 DB Amsterdam, The Netherlands*

[43] *University of Notre Dame, Notre Dame, Indiana 46556, USA*

[44] *Ohio State University, Columbus, Ohio 43210, USA*

[45a] *INFN Sezione di Padova, I-35131 Padova, Italy*

[45b] *Dipartimento di Fisica, Università di Padova, I-35131 Padova, Italy*

[46] *Laboratoire de Physique Nucléaire et de Hautes Energies, IN2P3/CNRS, Université Pierre et Marie*
*Curie-Paris6, Université Denis Diderot-Paris7, F-75252 Paris, France*

[47a] *INFN Sezione di Perugia, I-06123 Perugia, Italy*

[47b] *Dipartimento di Fisica, Università di Perugia, I-06123 Perugia, Italy*

[48a] *INFN Sezione di Pisa, I-56127 Pisa, Italy*

[48b] *Dipartimento di Fisica, Università di Pisa, I-56127 Pisa, Italy*

[48c] *Scuola Normale Superiore di Pisa, I-56127 Pisa, Italy*

[49] *Princeton University, Princeton, New Jersey 08544, USA*

[50a] *INFN Sezione di Roma, I-00185 Roma, Italy*

[50b] *Dipartimento di Fisica, Università di Roma La Sapienza, I-00185 Roma, Italy*

[51] *Universität Rostock, D-18051 Rostock, Germany*

[52] *Rutherford Appleton Laboratory, Chilton, Didcot, Oxon OX11 0QX, United Kingdom*

[53] *CEA, Irfu, SPP, Centre de Saclay, F-91191 Gif-sur-Yvette, France*

[54] *SLAC National Accelerator Laboratory, Stanford, California 94309 USA*

[55] *University of South Carolina, Columbia, South Carolina 29208, USA*

[56] *Southern Methodist University, Dallas, Texas 75275, USA*

[57] *Stanford University, Stanford, California 94305, USA*

[58] *State University of New York, Albany, New York 12222, USA*

[59] *Tel Aviv University, School of Physics and Astronomy, Tel Aviv, 69978, Israel*

[60] *University of Tennessee, Knoxville, Tennessee 37996, USA*

[61] *University of Texas at Austin, Austin, Texas 78712, USA*

[62] *University of Texas at Dallas, Richardson, Texas 75083, USA*

[63a]*INFN Sezione di Torino, I-10125 Torino, Italy*
[63b]*Dipartimento di Fisica, Università di Torino, I-10125 Torino, Italy*
[64]*INFN Sezione di Trieste and Dipartimento di Fisica, Università di Trieste, I-34127 Trieste, Italy*
[65]*IFIC, Universitat de Valencia-CSIC, E-46071 Valencia, Spain*
[66a]*Institute of Particle Physics, Victoria, British Columbia, Canada V8W 3P6*
[66b]*University of Victoria, Victoria, British Columbia, Canada V8W 3P6*
[67]*Department of Physics, University of Warwick, Coventry CV4 7AL, United Kingdom*
[68]*University of Wisconsin, Madison, Wisconsin 53706, USA*
(Received 6 February 2017; published 10 April 2017)

We study the processes $e^+e^- \to \gamma_{\text{ISR}}J/\psi$, where $J/\psi \to \pi^+\pi^-\pi^0$, $J/\psi \to K^+K^-\pi^0$, and $J/\psi \to K_S^0 K^\pm \pi^\mp$ using a data sample of 519 fb$^{-1}$ recorded with the *BABAR* detector operating at the SLAC PEP-II asymmetric-energy $e^+e^-$ collider at center-of-mass energies at and near the $\Upsilon(nS)$ ($n = 2, 3, 4$) resonances. We measure the ratio of branching fractions $\mathcal{R}_1 = \frac{\mathcal{B}(J/\psi \to K^+K^-\pi^0)}{\mathcal{B}(J/\psi \to \pi^+\pi^-\pi^0)}$ and $\mathcal{R}_2 = \frac{\mathcal{B}(J/\psi \to K_S^0 K^\pm \pi^\mp)}{\mathcal{B}(J/\psi \to \pi^+\pi^-\pi^0)}$. We perform Dalitz plot analyses of the three $J/\psi$ decay modes and measure fractions for resonances contributing to the decays. We also analyze the $J/\psi \to \pi^+\pi^-\pi^0$ decay using the Veneziano model. We observe structures compatible with the presence of $\rho(1450)$ in all three $J/\psi$ decay modes and measure the relative branching fraction: $\mathcal{R}(\rho(1450)) = \frac{\mathcal{B}(\rho(1450) \to K^+K^-)}{\mathcal{B}(\rho(1450) \to \pi^+\pi^-)} = 0.307 \pm 0.084(\text{stat}) \pm 0.082(\text{sys})$.

## I. INTRODUCTION

Charmonium decays, in particular radiative and hadronic decays of the $J/\psi$ meson, have been studied extensively [1,2]. One of the motivations for these studies is to search for non-$q\bar{q}$ mesons such as glueballs or molecular states that are predicted by QCD to populate the low mass region of the hadron mass spectrum [3].

Previous studies of $J/\psi$ decays to $\pi^+\pi^-\pi^0$ show a clear signal of $\rho(770)$ production [4,5]. In addition there is an indication of higher mass resonance production in $\psi(2S)$ decays [5]. This is not necessarily the case in $J/\psi$ decays, but neither does the $\rho(770)$ contribution saturate the spectrum. Attempts have been made to describe the $J/\psi$ decay distribution with additional partial waves [6]. It was found that interference effects are strong and even after adding $\pi\pi$ interactions up to $\approx 1.6$ GeV/$c^2$ the description remained quite poor. Continuing to expand the partial wave basis to cover an even higher mass region would lead to a rather unconstrained analysis. On the other hand with the amplitudes developed in the Veneziano model, all partial waves are related to the same Regge trajectory, which gives a very strong constraint on the amplitude analysis [7].

While large samples of $J/\psi$ decays exist, some branching fractions remain poorly measured. In particular the $J/\psi \to K^+K^-\pi^0$ branching fraction has been measured by Mark II [8] using only 25 events.

Only a preliminary result exists, to date, on a Dalitz plot analysis of $J/\psi$ decays to $\pi^+\pi^-\pi^0$ [9]. The BESII experiment [10] has performed an angular analysis of $J/\psi \to K^+K^-\pi^0$. The analysis requires the presence of a broad $J^{PC} = 1^{--}$ state in the $K^+K^-$ threshold region, which is interpreted as a multiquark state. However Refs. [11,12] explain it by the interference between the $\rho(1450)$ and $\rho(1700)$. On the other hand, the decay $\rho(1450) \to K^+K^-$ appears as "not seen" according to the PDG listing [13]. No Dalitz plot analysis has been performed to date on the $J/\psi \to K_S^0 K^\pm \pi^\mp$ decay.

We describe herein a study of the $J/\psi \to \pi^+\pi^-\pi^0$, $J/\psi \to K^+K^-\pi^0$, and $J/\psi \to K_S^0 K^\pm \pi^\mp$ decays produced in $e^+e^-$ annihilation via initial-state radiation (ISR), where only resonances with $J^{PC} = 1^{--}$ can be produced.

This article is organized as follows. In Sec. II, a brief description of the *BABAR* detector is given. Section III is devoted to the event reconstruction and data selection. In Sec. IV, we describe the study of efficiency and resolution, while Sec. V is devoted to the measurement of the $J/\psi$ branching fractions. Section VI describes the Dalitz plot analyses while in Sec. VII, we report the measurement of the $\rho(1450)$ branching fraction. Finally we summarize the results in Sec. VIII.

---
[*]Deceased.
[†]Also at Thomas Jefferson National Accelerator Facility, Newport News, Virginia 23606, USA.
[‡]Present address: Wuhan University, Wuhan 43072, China.
[§]Present address: Università di Bologna and INFN Sezione di Bologna, I-47921 Rimini, Italy.
[¶]Present address: University of Huddersfield, Huddersfield HD1 3DH, United Kingdom.
[**]Present address: University of South Alabama, Mobile, Alabama 36688, USA.
[††]Also at Università di Sassari, I-07100 Sassari, Italy.

## II. THE *BABAR* DETECTOR AND DATA SET

The results presented here are based on data collected with the *BABAR* detector at the PEP-II asymmetric-energy

$e^+e^-$ collider located at SLAC. The data sample corresponds to an integrated luminosity of 519 fb$^{-1}$ [14] recorded at center-of-mass energies at and near the $\Upsilon(nS)$ ($n = 2, 3, 4$) resonances. The *BABAR* detector is described in detail elsewhere [15]. Charged particles are detected, and their momenta are measured, by means of a five-layer, double-sided microstrip detector, and a 40-layer drift chamber, both operating in the 1.5 T magnetic field of a superconducting solenoid. Photons are measured and electrons are identified in a CsI(Tl) crystal electromagnetic calorimeter (EMC). Charged-particle identification is provided by the specific energy loss in the tracking devices, and by an internally reflecting ring-imaging Cherenkov detector. Muons are detected in the instrumented flux return of the magnet. Monte Carlo (MC) simulated events [16], with sample sizes more than 10 times larger than the corresponding data samples, are used to evaluate signal efficiency and to determine background features.

## III. EVENT RECONSTRUCTION AND DATA SELECTION

We study the following reactions:

$$e^+e^- \rightarrow \gamma_{\text{ISR}}\pi^+\pi^-\pi^0, \tag{1}$$

$$e^+e^- \rightarrow \gamma_{\text{ISR}}K^+K^-\pi^0, \tag{2}$$

$$e^+e^- \rightarrow \gamma_{\text{ISR}}K_S^0K^{\pm}\pi^{\mp}, \tag{3}$$

where $\gamma_{\text{ISR}}$ indicates the ISR photon.

For reactions (1) and (2), we consider only events for which the number of well-measured charged-particle tracks with transverse momenta greater than 0.1 GeV/$c$ is exactly equal to 2. The charged-particle tracks are fitted to a common vertex with the requirements that they originate from the interaction region and that the $\chi^2$ probability of the vertex fit be greater than 0.1%. We observe prominent $J/\psi$ signals in both reactions and optimize the signal-to-background ratio using the data by retaining only selection criteria that do not remove significant $J/\psi$ signal. We require the energy of the less-energetic photon from $\pi^0$ decays to be greater than 100 MeV. Each pair of photons is kinematically fitted to a $\pi^0$ requiring it to emanate from the primary vertex of the event, and with the diphoton mass constrained to the nominal $\pi^0$ mass [13]. Due to the soft-photon background, we do not impose a veto on the presence of additional photons in the final state but we require exactly one $\pi^0$ candidate in each event. Particle identification is used in two different ways. For reaction (1), we require two oppositely charged particles to be loosely identified as pions. For reaction (2), we loosely identify one kaon and require that neither track be a well-identified pion, electron, or muon.

For reaction (3), we consider only events for which the number of well-measured charged-particle tracks with

transverse momentum greater than 0.1 GeV/$c$ is exactly equal to 4, and for which there are no more than five photon candidates with reconstructed energy in the EMC greater than 100 MeV. We obtain $K_S^0 \rightarrow \pi^+\pi^-$ candidates by means of a vertex fit of pairs of oppositely charged tracks, for which we require a $\chi^2$ fit probability greater than 0.1%. Each $K_S^0$ candidate is then combined with two oppositely charged tracks, and fitted to a common vertex, with the requirements that the fitted vertex be within the $e^+e^-$ interaction region and have a $\chi^2$ fit probability greater than 0.1%. We select kaons and pions by applying high-efficiency particle identification criteria. We do not apply any particle identification requirements to the pions from the $K_S^0$ decay. We accept only $K_S^0$ candidates with decay lengths from the $J/\psi$ candidate decay vertex greater than 0.2 cm, and require $\cos \theta_{K_S^0} > 0.98$, where $\theta_{K_S^0}$ is defined as the angle between the $K_S^0$ momentum direction and the line joining the $J/\psi$ and $K_S^0$ vertices. A fit to the $\pi^+\pi^-$ mass spectrum using a linear function for the background and a Gaussian function with mean $m$ and width $\sigma$ gives $m = 497.24$ MeV/$c^2$ and $\sigma = 2.9$ MeV/$c^2$. We select the $K_S^0$ signal region to be within $\pm 2\sigma$ of $m$ and reconstruct the $K_S^0$ four-vector by summing the three-momenta of the pions and computing the energy using the known $K_S^0$ mass [13].

The ISR photon is preferentially emitted at small angles with respect to the beam axis (see Fig. 1), and escapes detection in the majority of ISR events. Consequently, the ISR photon is treated as a missing particle.

We define the squared mass $M_{\text{rec}}^2$ recoiling against the $\pi^+\pi^-\pi^0$, $K^+K^-\pi^0$, and $K_S^0K^{\pm}\pi^{\mp}$ systems using the four-momenta of the beam particles ($p_{e^{\pm}}$) and of the reconstructed final state particles:

$$M_{\text{rec}}^2 \equiv (p_{e^-} + p_{e^+} - p_{h_1} - p_{h_2} - p_{h_3})^2, \tag{4}$$

where the $h_i$ indicate the three hadrons in the final states. This quantity should peak near zero for both ISR events and
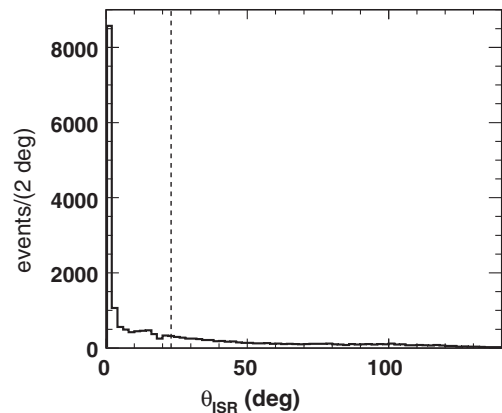


FIG. 1.   (a) Distribution of $\theta_{\text{ISR}}$ for events in the $J/\psi \rightarrow \pi^+\pi^-\pi^0$ ISR signal region. The dashed line indicates the $\theta_{\text{ISR}} = 23^0$ angle.

TABLE I. Ranges used to define the $J/\psi$ signal regions, event yields, and purities for the three $J/\psi$ decay modes.

| $J/\psi$ decay mode | Signal region (GeV/$c^2$) | Event yields | Purity % |
|---|---|---|---|
| $\pi^+\pi^-\pi^0$ | 3.028–3.149 | 20417 | $91.3 \pm 0.2$ |
| $K^+K^-\pi^0$ | 3.043–3.138 | 2102 | $88.8 \pm 0.7$ |
| $K_S^0 K^\pm \pi^\mp$ | 3.069–3.121 | 3907 | $93.1 \pm 0.4$ |

for exclusive production of $e^+e^- \rightarrow h_1 h_2 h_3$. However, in the exclusive production the $h_1 h_2 h_3$ mass distribution peaks at the kinematic limit. We select the ISR reactions (in the following also defined as ISR regions) requiring

$$|M_{\rm rec}^2| < 2 \text{ GeV}^2/c^4 \qquad (5)$$

for reaction (1) and (2) and

$$|M_{\rm rec}^2| < 1.5 \text{ GeV}^2/c^4 \qquad (6)$$

for reaction (3).

We reconstruct the three-momentum of the ISR photon from momentum conservation as

$$\mathbf{p}_{\rm ISR} = \mathbf{p}_{e^-} + \mathbf{p}_{e^+} - \mathbf{p}_{h_1} - \mathbf{p}_{h_2} - \mathbf{p}_{h_3}. \qquad (7)$$

Table I gives the ranges used to define the ISR signal regions for the three $J/\psi$ decay modes. We show in Fig. 1, for events in the $J/\psi \rightarrow \pi^+\pi^-\pi^0$ ISR signal region, the distribution of $\theta_{\rm ISR}$, the angle of the reconstructed ISR photon with respect to the $e^-$ beam direction in the laboratory system. We observe a narrow peak close to zero with a tail extending up to $140^0$ while background events from $J/\psi$ sidebands are distributed over the full angular range. Since angular coverage of the EMC starts at $\theta > 23^0$, we improve the signal to background ratio for $J/\psi$ events where $\theta_{\rm ISR} > 23^0$, by removing events for which no photon shower is found in the EMC in the expected angular region. Therefore, we require the difference between the predicted polar and azimuthal angles from $p_{\rm ISR}$ and the closest photon shower to be $|\Delta\theta| < 0.1$ rad and $|\Delta\phi| < 0.05$ rad. We do not use the information on the energy since some photons may not be fully contained in the EMC.

For reaction (1) we define the helicity angle $\theta_h$ as the angle in the $\pi^+\pi^-$ rest frame between the direction of the $\pi^+$ and the boost from the $\pi^+\pi^-$. We observe that residual background from $e^+e^- \rightarrow \gamma\pi^+\pi^-$ is concentrated at $|\cos\theta_\pi| \approx 1$ and therefore we remove events having $|\cos\theta_\pi| > 0.95$. A very small $J/\psi$ signal is observed in the events removed by this selection. No evidence is found for background from the ISR reaction $e^+e^- \rightarrow \gamma K^+K^-$.

Figure 2 shows the $M_{\rm rec}^2$ distributions for the three reactions in the $J/\psi$ signal regions, in comparison to the corresponding $M_{\rm rec}^2$ distributions obtained from simulation.
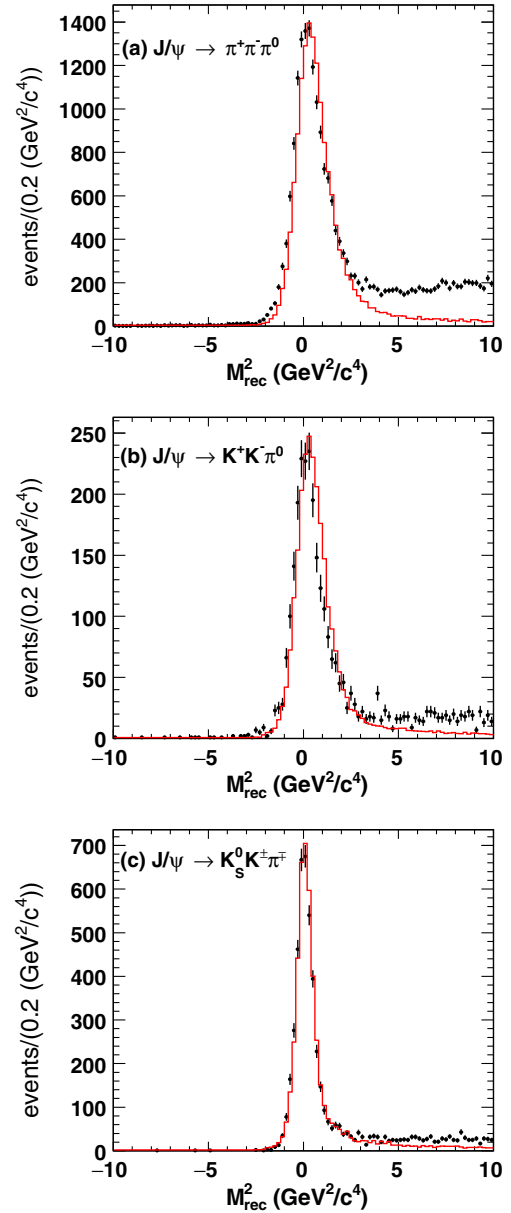


FIG. 2. Distributions of $M_{\rm rec}^2$ for $e^+e^- \rightarrow \gamma_{\rm ISR} J/\psi$, where (a) $J/\psi \rightarrow \pi^+\pi^-\pi^0$, (b) $J/\psi \rightarrow K^+K^-\pi^0$, and (c) $J/\psi \rightarrow K_S^0 K^\pm \pi^\mp$. In each figure the data are shown as points with error bars, and the MC simulation is shown as a histogram.

A peak at zero is observed in all distributions indicating the presence of the ISR process. We observe some discrepancy for reactions (1) and (2) due to some inaccuracy in reconstructing slow $\pi^0$ in the EMC. Figure 3 shows the $\pi^+\pi^-\pi^0$, $K^+K^-\pi^0$, and $K_S^0 K^\pm \pi^\mp$ mass spectra in the ISR region, before applying the efficiency correction. We observe strong $J/\psi$ signals over relatively small backgrounds and no more than one candidate per event. We perform a fit to the $\pi^+\pi^-\pi^0$, $K^+K^-\pi^0$, and $K_S^0 K^\pm \pi^\mp$ mass spectra. Backgrounds are described by first-order polynomials, and each resonance is represented by a simple
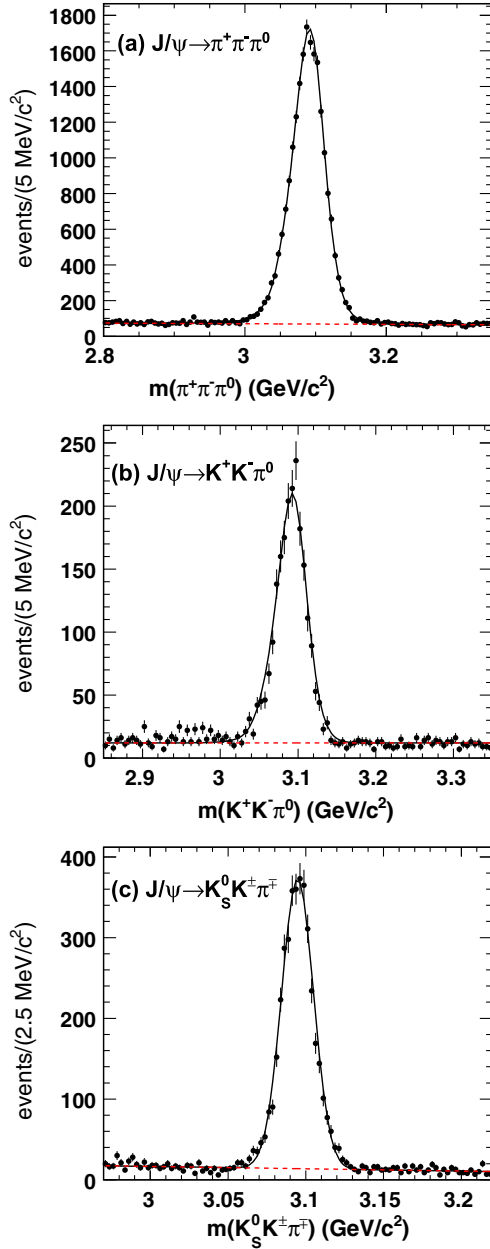
FIG. 3. (a) The $\pi^+\pi^-\pi^0$, (b) $K^+K^-K^0$, and $K_S^0 K^\pm \pi^\mp$ mass spectra in the ISR region. In each figure, the solid curve shows the total fit function and the dashed curve shows the fitted background contribution.

Breit-Wigner function convolved with the corresponding resolution function (see Sec. IV). Figure 3 shows the fit result, and Table II summarizes the mass values and yields. We observe (not taking into account systematic uncertainties) a $J/\psi$ mass shift of $+2.9$, $+4.1$, and $-2.2$ MeV/$c^2$ for the three decay modes.

## IV. EFFICIENCY AND RESOLUTION

To compute the efficiency, $J/\psi$ MC signal events for the three channels are generated using a detailed detector

TABLE II. Results from the fits to the mass spectra and efficiency corrections. Errors are statistical only.

| $J/\psi$ decay mode | $\chi^2/NDF$ | $J/\psi$ mass (MeV/$c^2$) | Signal yield | $1/\varepsilon$ |
|---|---|---|---|---|
| $\pi^+\pi^-\pi^0$ | 90/105 | 3099.8±0.2 | 19560±164 | 15.57±1.05 |
| $K^+K^-\pi^0$ | 129/95 | 3101.0±0.2 | 2002±48 | 18.31±0.63 |
| $K_S^0 K^\pm \pi^\mp$ | 127/96 | 3094.7±0.2 | 3694±64 | 15.15±0.33 |

simulation [16] in which the $J/\psi$ decays uniformly in phase space. These simulated events are reconstructed and analyzed in the same manner as data. The efficiency is computed as the ratio of reconstructed to generated events. We express the efficiency as a function of the $m_{12}$ mass ($\pi^+\pi^-$ for $J/\psi \to \pi^+\pi^-\pi^0$, $K^+K^-$ for $J/\psi \to K^+K^-\pi^0$, and $K_S^0 K^\pm$ for $J/\psi \to K_S^0 K^\pm \pi^\mp$) and $\cos\theta_h$ defined in Sec. III. To smooth statistical fluctuations, this efficiency is then parametrized as follows [17].

First we fit the efficiency as a function of $\cos\theta_h$ in separate intervals of $m_{12}$, in terms of Legendre polynomials up to $L = 12$:

$$\varepsilon(\cos\theta_h) = \sum_{L=0}^{12} a_L(m_{12}) Y_L^0(\cos\theta_h). \quad (8)$$

For each value of $L$, we fit the mass dependent coefficients $a_L(m_{12})$ with a seventh-order polynomial in $m_{12}$. Figure 4 shows the resulting fitted efficiency $\varepsilon(m_{12}, \cos\theta_h)$ for each of the three reactions. We observe a significant decrease in efficiency at low $m_{12}$ for $\cos\theta \sim \pm 1$ and $1.1 < m(K^+K^-) < 1.5$ GeV/$c^2$ due to the difficulty of reconstructing low-momentum tracks ($p < 200$ MeV/$c$ in the laboratory frame), which arise because of significant energy losses in the beampipe and inner-detector material.

The mass resolution, $\Delta m$, is measured as the difference between the generated and reconstructed $\pi^+\pi^-\pi^0$, $K^+K^-\pi^0$, and $K_S^0 K^\pm \pi^\mp$ invariant-mass values. These distributions, for the $J/\psi$ decays having a $\pi^0$ in the final state, deviate from Gaussian shapes due to a low-energy tail caused by the response of the CsI calorimeter to photons. We fit the distributions using the sum of a Crystal Ball function [18] and a Gaussian function. The root-mean-squared values are 24.4 and 22.7 MeV/$c^2$ for the $J/\psi \to \pi^+\pi^-\pi^0$ and $J/\psi \to K^+K^-\pi^0$ final states, respectively. The mass resolution for $J/\psi \to K_S^0 K^\pm \pi^\mp$ is well described by a single Gaussian having a $\sigma = 9.7$ MeV/$c^2$.

## V. $J/\psi$ BRANCHING RATIOS

We compute the ratio of the branching fractions for $J/\psi \to K^+K^-\pi^0$ and $J/\psi \to \pi^+\pi^-\pi^0$ according to

$$\mathcal{R}_1 = \frac{\mathcal{B}(J/\psi \to K^+K^-\pi^0)}{\mathcal{B}(J/\psi \to \pi^+\pi^-\pi^0)} = \frac{N_{K^+K^-\pi^0}}{N_{\pi^+\pi^-\pi^0}} \frac{\varepsilon_{\pi^+\pi^-\pi^0}}{\varepsilon_{K^+K^-\pi^0}}, \quad (9)$$

## (a) $J/\psi \to \pi^+\pi^-\pi^0$



## (b) $J/\psi \to K^+K^-\pi^0$



## (c) $J/\psi \to K^0_S K^\pm \pi^\mp$
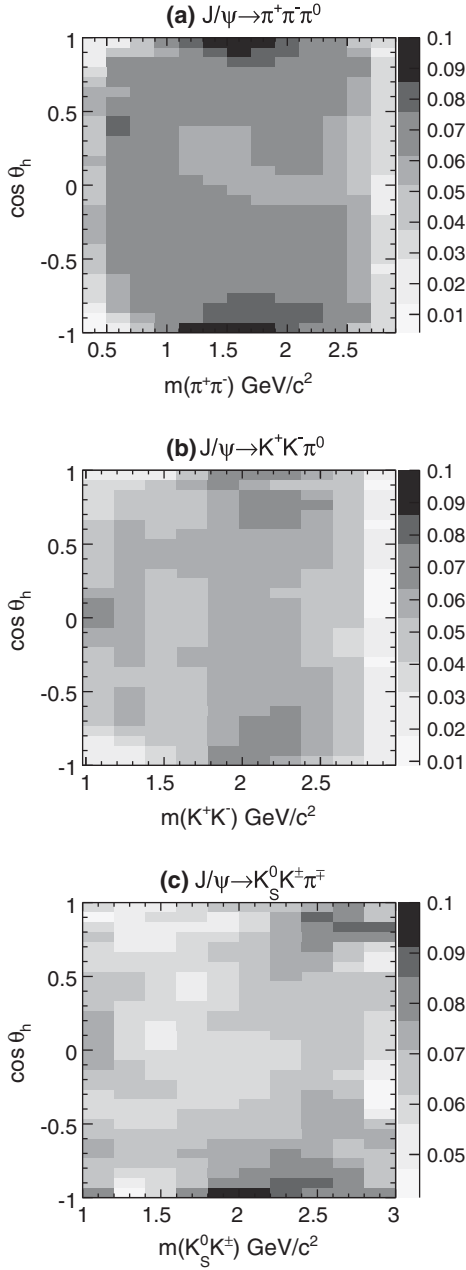


FIG. 4.    Fitted detection efficiency in the $\cos\theta_h$ vs $m_{12}$ plane for (a) $J/\psi \to \pi^+\pi^-\pi^0$, (b) $J/\psi \to K^+K^-\pi^0$, and (c) $J/\psi \to K^0_S K^\pm \pi^\mp$. Each bin shows the average value of the fit in that region.

by assigning a weight $w = f/\varepsilon(m_{12}, \cos\theta)$, where $f = 1$ for events in the $J/\psi$ signal region and $f = -1$ for events in the sideband regions. The size of the sum of the two sidebands is taken to be the same as that of the signal region. Therefore we obtain the weighted efficiencies as

$$\varepsilon_{h^+h^-\pi^0} = \frac{\sum_{i=1}^{N} f_i}{\sum_{i=1}^{N} f_i/\varepsilon(m_{12}, \cos\theta_i)}, \qquad (10)$$

where $N$ indicates the number of events in the signal + sidebands regions. The resulting yields and efficiencies are reported in Table II.

We note that in Eq. (9) the number of charged-particle tracks and $\gamma$'s is the same in the numerator and in the denominator of the ratio, so that several systematic uncertainties cancel. We estimate the systematic uncertainties as follows. We modify the signal fitting function, describing the $J/\psi$ signals using the sum of two Gaussian functions. The uncertainty due to efficiency weighting is evaluated by computing 1000 new weights obtained by randomly modifying the weight in each cell of the $\varepsilon(m_{12}, \cos\theta)$ plane according to its statistical uncertainty. The widths of the resulting Gaussian distributions yield the estimate of the systematic uncertainty for the efficiency weighting procedure. These values are reported as the uncertainties on $1/\varepsilon$ in Table II. We assign a 1% systematic uncertainty for the identification of each of the two kaons, from studies performed using high statistics control samples. The contributions to the systematic uncertainties from different sources are given in Table III and combined in quadrature. We obtain

$$\begin{aligned} \mathcal{R}_1 &= \frac{\mathcal{B}(J/\psi \to K^+K^-\pi^0)}{\mathcal{B}(J/\psi \to \pi^+\pi^-\pi^0)} \\ &= 0.120 \pm 0.003(\text{stat}) \pm 0.009(\text{sys}). \qquad (11) \end{aligned}$$

The PDG reports $\mathcal{B}(J/\psi \to \pi^+\pi^-\pi^0) = (2.11 \pm 0.07) \times 10^{-2}$, while the branching fraction $\mathcal{B}(J/\psi \to K^+K^-\pi^0)$ has been measured by Mark II [8] using 25 events, to be $(2.8 \pm 0.8) \times 10^{-3}$. These values give a ratio $\mathcal{R}_1^{\text{PDG}} = 0.133 \pm 0.038$, in agreement with our measurement.

TABLE III.    Fractional systematic uncertainties in the evaluation of the ratios of branching fractions.

| Effect | $\mathcal{R}_1$ (%) | $\mathcal{R}_2$ (%) |
|---|---|---|
| Efficiency | 7.5 | 7.0 |
| Background subtraction | 1.3 | 1.0 |
| Particle identification | 2.0 | 1.8 |
| $K^0_S$ reconstruction | | 1.1 |
| $\pi^0$ reconstruction | | 3.0 |
| Mass fits | 0.8 | 0.8 |
| Total | 7.9 | 8.0 |

where $N_{\pi^+\pi^-\pi^0}$ and $N_{K^+K^-\pi^0}$ represent the fitted yields for $J/\psi$ in the $\pi^+\pi^-\pi^0$ and $K^+K^-\pi^0$ mass spectra, while $\varepsilon_{\pi^+\pi^-\pi^0}$ and $\varepsilon_{K^+K^-\pi^0}$ are the corresponding efficiencies. We estimate $\varepsilon_{\pi^+\pi^-\pi^0}$ and $\varepsilon_{K^+K^-\pi^0}$ for the $J/\psi$ signals by making use of the 2D efficiency distributions described in Sec. IV. To remove the dependence of the fit quality on the efficiency functions we make use of the unfitted efficiency distributions. Due to the presence of non-negligible backgrounds in the $J/\psi$ signals, which have different distributions in the Dalitz plot, we perform a sideband subtraction

We perform a test of the $\mathcal{R}_1$ measurement using a minimum bias procedure. We remove all the selections used to separate reactions (1) and (2), except for the requirements on $M_{\text{rec}}^2$ and obtain the events yield for $J/\psi \to \pi^+\pi^-\pi^0$. To obtain the $J/\psi \to K^+K^-\pi^0$ yield, we apply very loose identifications of the two kaons to remove the large background and the strong cross feed from the $J/\psi \to \pi^+\pi^-\pi^0$ final state. We observe a loss of the $J/\psi$ signal which is estimated by MC to be 3.6%. The ratios between the two minimum bias yields, corrected for the above efficiency loss gives directly the ratio of the two branching fractions which is in good agreement with the previous estimate.

Using a similar procedure as for the measurement of $\mathcal{R}_1$, correcting for unseen $K_S^0$ decay modes, we compute the ratio of the branching fractions for $J/\psi \to K_S^0 K^\pm \pi^\mp$ and $J/\psi \to \pi^+\pi^-\pi^0$ according to

$$
\begin{aligned}
\mathcal{R}_2 &= \frac{\mathcal{B}(J/\psi \to K_S^0 K^\pm \pi^\mp)}{\mathcal{B}(J/\psi \to \pi^+\pi^-\pi^0)} \\
&= \frac{N_{K_S^0 K^\pm \pi^\mp}}{N_{\pi^+\pi^-\pi^0}} \frac{\varepsilon_{\pi^+\pi^-\pi^0}}{\varepsilon_{K_S^0 K^\pm \pi^\mp}} \\
&= 0.265 \pm 0.005(\text{stat}) \pm 0.021(\text{sys}). \quad (12)
\end{aligned}
$$

Systematic uncertainties on the evaluation of $\mathcal{R}_2$ include 0.46% per track for charged tracks reconstruction, 3% and 1.1% for $\pi^0$ and $K_S^0$ reconstruction, and 0.5% and 1% for the identification of pions and kaons, respectively. The contributions to the total systematic uncertainty are summarized in Table III.

The branching fraction $\mathcal{B}(J/\psi \to K_S^0 K^\pm \pi^\mp)$ has been measured by Mark I [19], using 126 events, to be $(26 \pm 7) \times 10^{-4}$. Using the above measurements we obtain an estimate of $\mathcal{R}_2$:

$$
\mathcal{R}_2^{\text{PDG}} = 0.123 \pm 0.033, \quad (13)
$$

which deviates by $3.6\sigma$ from our measurement.

As a cross-check, using the above $\mathcal{R}_1$ and $\mathcal{R}_2$ measurements and adding in quadrature statistical and systematic uncertainties, we compute

$$
\mathcal{R}_3 = \frac{\mathcal{B}(J/\psi \to K_S^0 K^\pm \pi^\mp)}{\mathcal{B}(J/\psi \to K^+K^-\pi^0)} = 2.21 \pm 0.24 \quad (14)
$$

in agreement with the expected value of 2.

## VI. DALITZ PLOT ANALYSIS

We perform Dalitz plot analyses of the $J/\psi \to \pi^+\pi^-\pi^0$, $J/\psi \to K^+K^-\pi^0$, and $J/\psi \to K_S^0 K^\pm \pi^\mp$ candidates in the $J/\psi$ mass region using unbinned maximum likelihood fits. The likelihood function is written as

$$
\begin{aligned}
\mathcal{L} = \prod_{n=1}^{N} &\bigg[ f_{\text{sig}}(m_n) \cdot \varepsilon(x_n', y_n') \frac{\sum_{i,j} c_i c_j^* A_i(x_n, y_n) A_j^*(x_n, y_n)}{\sum_{i,j} c_i c_j^* I_{A_i A_j^*}} \\
&+ (1 - f_{\text{sig}}(m_n)) \frac{\sum_i k_i B_i(x_n, y_n)}{\sum_i k_i I_{B_i}} \bigg],
\end{aligned} \quad (15)
$$

where

(i) $N$ is the number of events in the signal region;

(ii) for the $n$th event, $m_n$ is the $\pi^+\pi^-\pi^0$, $K^+K^-\pi^0$, or $K_S^0 K^\pm \pi^\mp$ invariant mass;

(iii) for the $n$th event, $x_n = m^2(\pi^+\pi^0)$, $y_n = m^2(\pi^-\pi^0)$ for $\pi^+\pi^-\pi^0$; $x_n = m^2(K^+\pi^0)$, $y_n = m^2(K^-\pi^0)$ for $K^+K^-\pi^0$; $x_n = m^2(K^\pm\pi^\mp)$, $y_n = m^2(K_S^0\pi^\mp)$ for $K_S^0 K^\pm \pi^\mp$;

(iv) $f_{\text{sig}}$ is the mass-dependent fraction of signal obtained from the fits to the $\pi^+\pi^-\pi^0$, $K^+K^-\pi^0$, and $K_S^0 K^\pm \pi^\mp$ mass spectra;

(v) for the $n$th event, $\varepsilon(x_n', y_n')$ is the efficiency parametrized as a function $x_n' = m_{12}$ and $y_n' = \cos\theta_h$ (see Sec. IV);

(vi) for the $n$th event, the $A_i(x_n, y_n)$ represent the complex signal-amplitude contributions described below;

(vii) $c_i$ is the complex amplitude of the $i$th signal component; the $c_i$ parameters are allowed to vary during the fit process;

(viii) for the $n$th event, the $B_i(x_n, y_n)$ describe the background probability-density functions assuming that interference between signal and background amplitudes can be ignored;

(ix) $k_i$ is the magnitude of the $i$th background component; the $k_i$ parameters are obtained by fitting the sideband regions;

(x) $I_{A_i A_j^*} = \int A_i(x, y) A_j^*(x, y) \varepsilon(m_{12}, \cos\theta) dx dy$ and $I_{B_i} = \int B_i(x, y) dx dy$ are normalization integrals; numerical integration is performed on phase-space-generated events with $J/\psi$ signal and background generated according to the experimental distributions.

Parity conservation in $J/\psi \to \pi^+\pi^-\pi^0$ restricts the possible spin-parity of any intermediate two-body resonance to be $J^{PC} = 1^{--}, 3^{--}, \ldots$. Amplitudes are parametrized using Zemach's tensors [20,21]. Except as noted, all fixed resonance parameters are taken from the Particle Data Group averages [13].

For reaction (1), we label the decay particles as

$$
J/\psi \to \pi_1^+ \pi_2^- \pi_3^0. \quad (16)
$$

Indicating with $p_i$ the momenta of the particles in the $J/\psi$ center-of-mass rest frame, for a resonance $R_{jk}$ decaying as $R_{jk} \to j + k$ we also define the three-vectors $t_i$ as the vector part of

$$
t_i^\mu = p_j^\mu - p_k^\mu - (p_j^\mu + p_k^\mu) \frac{m_j^2 - m_k^2}{m_{jk}^2}, \quad (17)
$$

TABLE IV.   Amplitudes considered in $J/\psi \to \pi^+\pi^-\pi^0$, $J/\psi \to K^+K^-\pi^0$, and $J/\psi \to K_S^0 K^\pm \pi^\mp$ Dalitz plot analysis. BW indicates the Breit-Wigner function.

| $J/\psi$ decay mode | Decay | Amplitude |
|---|---|---|
| $\pi^+\pi^-\pi^0$ | $\rho\pi$ | $\mathrm{BW}_\rho(m_{13})(\mathbf{t_2}\times\mathbf{p_2})+\mathrm{BW}_\rho(m_{23})(\mathbf{t_1}\times\mathbf{p_1})+\mathrm{BW}_\rho(m_{12})(\mathbf{t_3}\times\mathbf{p_3})$ |
|  | NR | $(\mathbf{t_1}\times\mathbf{p_1})+(\mathbf{t_2}\times\mathbf{p_2})+(\mathbf{t_3}\times\mathbf{p_3})$ |
| $K\bar{K}\pi$ | $K^*\bar{K}$ | $\mathrm{BW}_{K^*}(m_{13})(\mathbf{t_2}\times\mathbf{p_2})+\mathrm{BW}_{K^*}(m_{23})(\mathbf{t_1}\times\mathbf{p_1})$ |
|  | $K_2^*(1430)\bar{K}$ | $\mathrm{BW}_{K_2^*}(m_{13})(\mathbf{k_2})+\mathrm{BW}_{K_2^*}(m_{23})(\mathbf{k_1})$ |
|  | $\rho\pi$ | $\mathrm{BW}_\rho(m_{12})(\mathbf{t_3}\times\mathbf{p_3})$ |

with $i, j, k$ cyclic. We make use of the $p_i$ vectors to describe the angular momentum $L$ between $R_{jk}$ and particle $i$, and the $t_i$ vectors to describe the spin of the $R_{jk}$ resonance. Since the $J/\psi$ resonance has spin-1 and needs to be described by a vector, the only way to obtain this result is to perform a cross-product between the $p_i$ and $t_i$ three-vectors. Indicating with $\rho$ a generic spin-1 resonance, Table IV reports the list of amplitudes used to describe the $J/\psi$ decays. Due to Bose symmetry, the amplitudes are symmetrized with respect to the $\rho$ charge. The Table also reports the expression for the nonresonant contribution (NR) which should also have the $J/\psi$ quantum numbers.

For reaction (2), we label the decay particles as

$$J/\psi \to K_1^+ K_2^- \pi_3^0. \qquad (18)$$

In this case two separate contributions are listed in Table IV, one in which the intermediate resonance is a $K^{*\pm} \to K^\pm\pi^0$ and the other where the intermediate resonance is a $\rho^0 \to K^+K^-$. The Table also lists the amplitude for the $K_2^*(1430)^\pm K^\mp$ contribution. This decay mode can only occur in D-wave. To obtain this amplitude, we construct rank-2 tensors $\mathbf{T_i} = t_i^j t_i^k - |t_i|^2 \delta^{jk}/3$ to describe the spin-2 of the $K_2^*(1430)^\pm$ resonance and $\mathbf{P_i} = p_i^j p_i^k - |p_i|^2 \delta^{jk}/3$ to describe the angular momentum between the $K_2^*(1430)^\pm$ and the $K^\mp$. The two rank-2 tensors are then contracted into vectors $\mathbf{k_i}$ to obtain the spin of the $J/\psi$ resonance. We obtain the components of $\mathbf{k_i}$ as $k_i^l = \sum_{\lambda=1}^{\lambda=3} T_i^{m,\lambda} P_i^{\lambda,n} - T_i^{n,\lambda} P_i^{\lambda,m}$ with $l, m, n$ cyclic [22].

The amplitudes for reaction (3) are similar to those from reaction (2). In this case we label the decay particles as

$$J/\psi \to K_1^\pm K_{S2}^0 \pi_3^\mp. \qquad (19)$$

The efficiency-corrected fractional contribution $f_i$ due to resonant or nonresonant contribution $i$ is defined as follows:

$$f_i = \frac{|c_i|^2 \int |A_i(x_n, y_n)|^2 \mathrm{d}x\mathrm{d}y}{\int |\sum_j c_j A_j(x, y)|^2 \mathrm{d}x\mathrm{d}y}. \qquad (20)$$

The $f_i$ do not necessarily sum to 100% because of interference effects. The uncertainty for each $f_i$ is evaluated

by propagating the full covariance matrix obtained from the fit.

Similarly, the efficiency-corrected interference fractional contribution $f_{ij}$, for $i < j$ are defined as

$$f_{ij} = \frac{\int 2\mathcal{R}e[c_i c_j^* A_i(x_n, y_n) A_j(x_n, y_n)^*]\mathrm{d}x\mathrm{d}y}{\int |\sum_j c_j A_j(x, y)|^2 \mathrm{d}x\mathrm{d}y}. \qquad (21)$$

In all the Dalitz analyses described below we validate the fitting algorithms using MC simulations with known input amplitudes and phases. We also start the fitting procedure both on MC and data from random values. In all cases the fits converge towards one single solution.

### A. Dalitz plot analysis of $J/\psi \to \pi^+\pi^-\pi^0$

#### 1. Isobar model

We perform a Dalitz plot analysis of $J/\psi \to \pi^+\pi^-\pi^0$ in the $J/\psi$ signal region given in Table I. This region contains 20417 events with $(91.3 \pm 0.2)\%$ purity, defined as $S/(S + B)$, where $S$ and $B$ indicate the number of signal and background events, respectively, as determined from the fit to the $\pi^+\pi^-\pi^0$ mass spectrum shown in Fig. 3(a). Sideband regions are defined as the ranges $2.919$–$2.980\,\mathrm{GeV}/c^2$ and $3.198$–$3.258\,\mathrm{GeV}/c^2$, respectively.
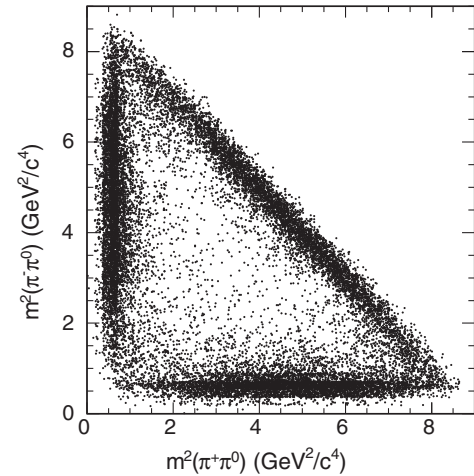


FIG. 5.   Dalitz plot for the $J/\psi \to \pi^+\pi^-\pi^0$ events in the signal region.
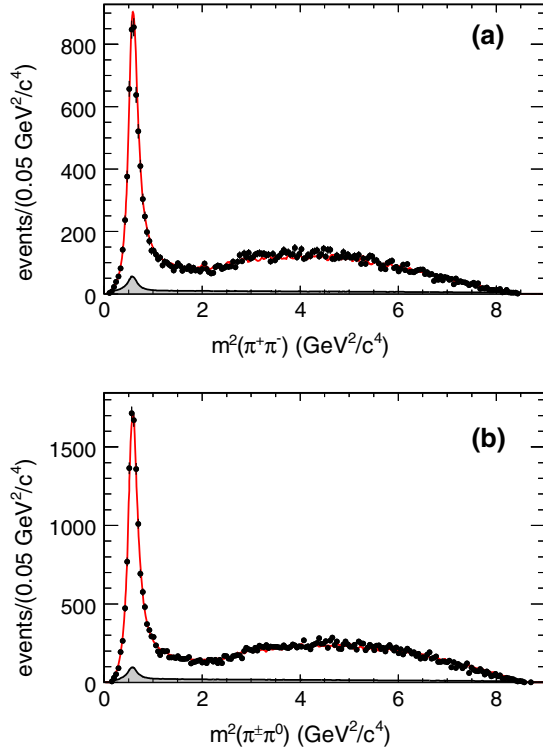
FIG. 6. The $J/\psi \to \pi^+\pi^-\pi^0$ Dalitz plot projections. The superimposed curves result from the Dalitz plot analysis described in the text. The shaded regions show the background estimates obtained by interpolating the results of the Dalitz plot analyses of the sideband regions.

Figure 5 shows the Dalitz plot for the $J/\psi$ signal region and Fig. 6 shows the Dalitz plot projections. We observe that the decay is dominated by $\rho(770)\pi$ amplitudes which appear as nonuniform bands along the Dalitz plot boundaries.

We first perform separate fits to the $J/\psi$ sidebands with an incoherent sum of amplitudes using the method of the channel likelihood [23]. We find significant contributions from $\rho(770)$ resonances with uniform distributions of events along their bands, as well as from an incoherent uniform background. The resulting amplitude fractions are interpolated into the $J/\psi$ signal region and normalized to

the fitted purity. Figure 6 shows the projections of the estimated background contributions as shaded.

For the description of the $J/\psi$ Dalitz plot, amplitudes are added one at a time to ascertain the associated increase of the likelihood value and decrease of the 2D $\chi^2$ computed on the $(m(\pi^+\pi^-), \cos\theta_h)$ plane. We test the quality of the fit by examining a large sample of MC events at the generator level weighted by the likelihood fitting function and by the efficiency. These events are used to compare the fit result to the Dalitz plot and its projections with proper normalization. The latter comparison is shown in Fig. 6, and good agreement is obtained for all projections. We make use of these weighted events to compute a 2D $\chi^2$ over the Dalitz plot. For this purpose, we divide the Dalitz plot into a number of cells such that the expected population in each cell is at least five events. We compute $\chi^2 = \sum_{i=1}^{N_{\text{cells}}}(N_{\text{obs}}^i - N_{\text{exp}}^i)^2/N_{\text{exp}}^i$, where $N_{\text{obs}}^i$ and $N_{\text{exp}}^i$ are event yields from data and simulation, respectively.

We leave free in the fit the $\rho(770)$ parameters and obtain results which are consistent with PDG averages [13]. We also leave free the $\rho(1450)$ and $\rho(1700)$ parameters in the fit and obtain a significant improvement of the likelihood with the following resonances parameters:

$$m(\rho(1450)) = 1429 \pm 41 \text{ MeV}/c^2,$$
$$\Gamma(\rho(1450)) = 576 \pm 29 \text{ MeV},$$
$$m(\rho(1700)) = 1644 \pm 36 \text{ MeV}/c^2,$$
$$\Gamma(\rho(1700)) = 109 \pm 19 \text{ MeV}. \quad (22)$$

We also test the presence of the isospin violating decay $\omega \to \pi^+\pi^-$. We notice that the $\omega(782)\pi^0$ contribution has a rather small fraction $(0.08 \pm 0.03)$ but its fitted amplitude is $(0.013 \pm 0.002)$. To obtain the statistical significance for this contribution, we remove the $\omega(782)\pi^0$ amplitude. We obtain $\Delta(-2\log L) = 27.7$ and $\Delta\chi^2 = 17$ for the difference of two parameters which corresponds to a significance of $4.9\sigma$. We also include the spin-3 $\rho_3(1690)\pi$ contribution but it is found consistent with zero.

Table V summarizes the fit results for the amplitude fractions and phases. We note that the $\rho(770)\pi$ amplitude

TABLE V. Results from the Dalitz plot analysis of the $J/\psi \to \pi^+\pi^-\pi^0$ channel. When two uncertainties are given, the first is statistical and the second systematic. The error on the amplitude is only statistical.

| Final state | Amplitude | Isobar fraction (%) | Phase (radians) | Veneziano fraction (%) |
|---|---|---|---|---|
| $\rho(770)\pi$ | 1.0 | $114.2 \pm 1.1 \pm 2.6$ | 0.0 | $133.1 \pm 3.3$ |
| $\rho(1450)\pi$ | $0.513 \pm 0.039$ | $10.9 \pm 1.7 \pm 2.7$ | $-2.63 \pm 0.04 \pm 0.06$ | $0.80 \pm 0.27$ |
| $\rho(1700)\pi$ | $0.067 \pm 0.007$ | $0.8 \pm 0.2 \pm 0.5$ | $-0.46 \pm 0.17 \pm 0.21$ | $2.20 \pm 0.60$ |
| $\rho(2150)\pi$ | $0.042 \pm 0.008$ | $0.04 \pm 0.01 \pm 0.20$ | $1.70 \pm 0.21 \pm 0.12$ | $6.00 \pm 2.50$ |
| $\omega(783)\pi^0$ | $0.013 \pm 0.002$ | $0.08 \pm 0.03 \pm 0.02$ | $2.78 \pm 0.20 \pm 0.31$ | |
| $\rho_3(1690)\pi$ | | | | $0.40 \pm 0.08$ |
| Sum | | $127.8 \pm 2.0 \pm 4.3$ | | $142.5 \pm 2.8$ |
| $\chi^2/\nu$ | | $687/519 = 1.32$ | | $596/508 = 1.17$ |

provides the largest contribution. We also observe an important contribution from the $\rho(1450)\pi$ amplitude, while the contributions from higher $\rho'$ resonances are small. We also notice that the $\rho(1700)\pi$ amplitude is significant even if the resulting fraction is very small, which can be attributed to the presence of important interference effects.

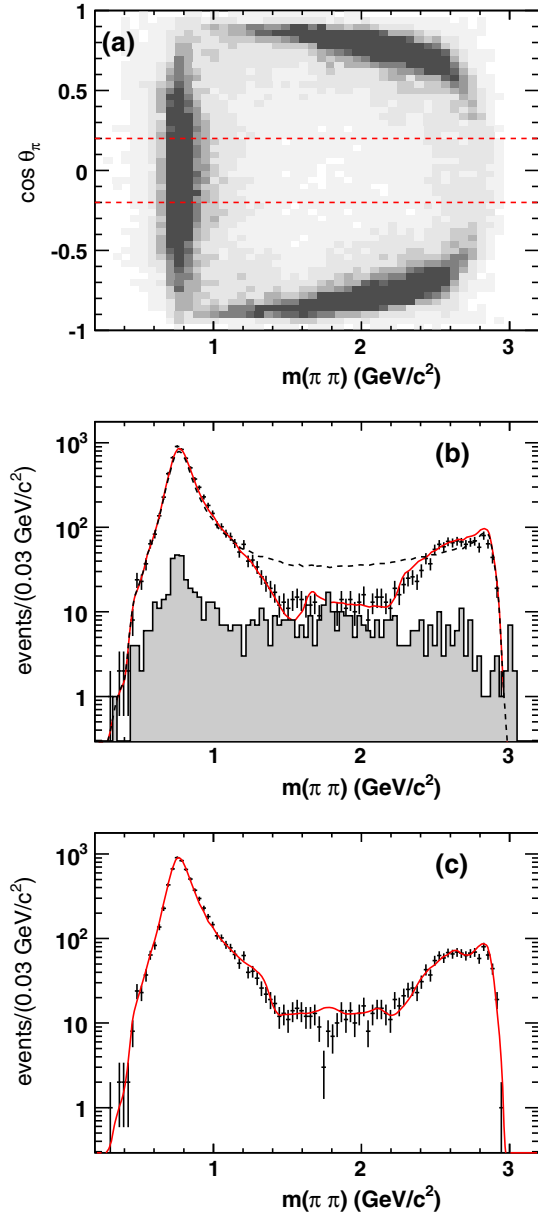To illustrate the contributions from higher $\rho$ states, we plot in Fig. 7(a), a binned scatter diagram of the helicity



FIG. 7.   (a) Binned scatter diagram of $\cos\theta_{\pi_3}$ vs $m(\pi_1\pi_2)$. (b) and (c) $\pi\pi$ mass projection in the $|\cos\theta_\pi| < 0.2$ region for all the three $\pi\pi$ charge combinations. The horizontal lines in (a) indicate the $\cos\theta_\pi$ selection. The dashed line in (b) is the result from the fit with only the $\rho(770)\pi$ amplitude. The fit in (b) uses the isobar model and the shaded histogram shows the background distribution estimated from the $J/\psi$ sidebands. The fit in (c) uses the Veneziano model.

angle $\theta_{\pi_3}$ vs $\pi_1\pi_2$ mass for the three possible combinations. The curved bands on the top and bottom are reflections from the other combinations. Selecting events $|\cos\theta_\pi| < 0.2$ almost completely removes these reflections and gives a more clear representation of the $\pi\pi$ mass spectrum, shown in Fig. 7(b) with a logarithmic scale for the sum of the three $\pi\pi$ mass combinations. We also compare the fit projections with the results from a fit where only the $\rho(770)\pi$ contribution is included. The distribution shows clearly the presence of higher excited $\rho$ resonances contributing to the $J/\psi \to \pi^+\pi^-\pi^0$ decay.

The NR contribution has been included but does not improve the fit quality. The sum of the fractions is significantly different from 100%. Denoting by $n(=8)$ the number of free parameters in the fit, we obtain $\chi^2/\nu = 687/519$ ($\nu = N_{\text{cells}} - n$).

We compute the uncorrected Legendre polynomial moments $\langle Y_L^0 \rangle$ in each $\pi^+\pi^-$ and $\pi^\pm\pi^0$ mass interval by weighting each event by the relevant $Y_L^0(\cos\theta_h)$ function. These distributions are shown in Figs. 8 and 9. We also compute the expected Legendre polynomial moments from the weighted MC events and compare with the experimental distributions. We observe a reasonable agreement for all the distributions, which indicates that the fit is able to reproduce most of the local structures apparent in the Dalitz plot. We also notice a few discrepancies in the high $\pi\pi$ mass region indicating the possible presence of additional unknown excited $\rho\pi$ contributions not included in the present analysis.

Systematic uncertainty estimates for the fractions and relative phases are computed in different ways.

  (i)  The purity function is scaled up and down by its statistical uncertainty.
 (ii)  The parameters of each resonance contributing to the decay are modified within one standard deviation of their uncertainties in the PDG averages.
(iii)  The Blatt-Weisskopf [24] factors entering in the relativistic Breit-Wigner function have been fixed to 1.5 $(\text{GeV}/c)^{-1}$ and varied between 1 and 4 $(\text{GeV}/c)^{-1}$.
 (iv)  We make use of the efficiency distribution without the smoothing described in Sec. IV.
  (v)  To estimate possible bias, we generate and fit MC simulated events according to the Dalitz plot fitted results.

The different contributions are added in quadrature in Table V.

### 2. Veneziano model

The particular approach used in this analysis follows recent work described in Ref. [7]. The dynamical assumptions behind the Veneziano model are the resonance dominance of the low-energy spectrum and resonance-Regge duality. The latter means that all resonances are
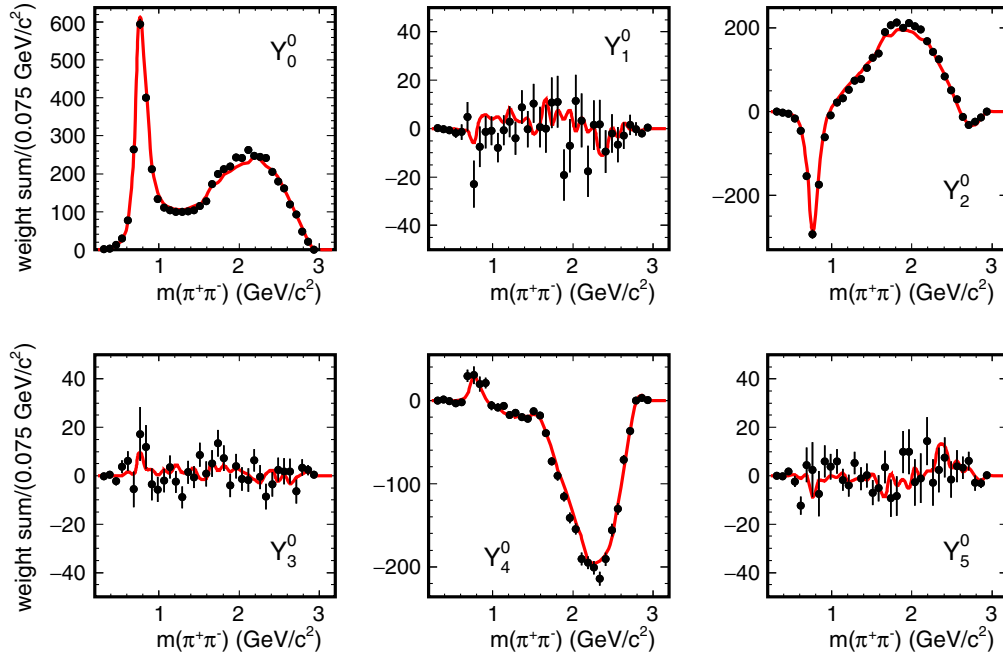
FIG. 8.  Legendre polynomial moments for $J/\psi \rightarrow \pi^+\pi^-\pi^0$ as a function of $\pi^+\pi^-$ mass. The superimposed curves result from the Dalitz plot analysis described in the text.
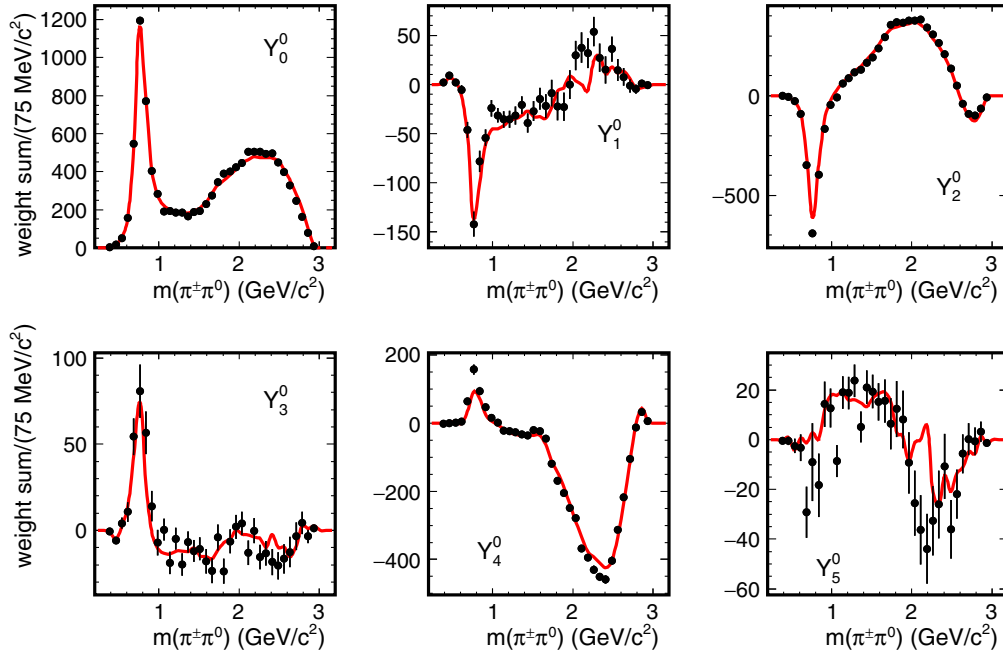


FIG. 9.  Legendre polynomial moments for $J/\psi \rightarrow \pi^+\pi^-\pi^0$ as a function of $\pi^{\pm}\pi^0$ mass. The superimposed curves result from the Dalitz plot analysis described in the text. The corresponding $\pi^+\pi^0$ and $\pi^-\pi^0$ distributions are combined.

located on Regge trajectories and that Regge poles are the only singularities of partial waves in the complex angular momentum plane. Therefore, there are no "unaccounted for" backgrounds and the Veneziano amplitude is used to fully describe the given reaction. A single Veneziano amplitude of the type

$$A_{n,m} = \frac{\Gamma(n - \alpha(s))\Gamma(n - \alpha(t))}{\Gamma(n + m - \alpha(s) - \alpha(t))} \quad (23)$$

has "predetermined" resonance strengths. Here $\alpha$ is the Regge trajectory, $s$ and $t$ are the Mandelstam variables and $n, m$ are integers. The position of resonances is determined

by poles of the amplitude, i.e. resonances in the $s(t)$-channel are determined by poles of the first (second) $\Gamma$ function in the numerator, respectively. Resonance couplings are determined by residues of the amplitude at the poles. In the model these are therefore determined by the properties of the $\Gamma$ function and the form of the Regge trajectory. Which resonances are excited depends, however, on the quantum numbers of external particles. Thus the amplitude in Eq. (23) should be considered as a building block rather than a physical amplitude. The latter is obtained by forming a linear combination of the $A_{n,m}$'s with parameters that are reaction dependent, i.e. fitted to the data. e.g.

$$A_{X \to abc} = \sum_{n,m} c_{X \to abc}(n,m) A_{n,m}. \qquad (24)$$

In this analysis a modified set of amplitudes $A_{n,m}$, which incorporate complex trajectories were used. Unlike the isobar model, the Veneziano model describes an infinite number of resonances. The resonances are not independent, the correlation between resonance masses, $m_R$ and spins $J_R$ is described by the Regge trajectory function $\alpha(s)$ such that $\alpha(m_R^2) = J_R$. Once the parameters $c$ in Eq. (24) are determined by fitting data, it is possible to compute the coupling constants of resonances to the external particles. Weak resonances may not be apparent in the data. They however are analytically connected to other, stronger resonances and determining the latter helps to constrain the couplings to the former. For example, the $\rho_3$ meson is expected to lie on the same Regge trajectory as the $\rho$. Thus coupling of the $\rho$ in $J/\psi \to \rho\pi \to 3\pi$ determines coupling of the $J/\psi$ to the $\rho_3$.

In the Veneziano model the complexity of the model is related to $n$ which is related to the number of Regge trajectories included in the fit. The number of free parameters also increases with $n$. The integer $m$ in Eq. (23) is related to the number of daughter trajectories and it is restricted by $1 \leq m \leq n$. The lower limit on $m$ guarantees that $J/\psi$ decay amplitude has the expected high-energy behavior and the upper limit eliminates double poles in overlapping channels. We fit the data varying $n$ from 1 to 8 and test the improvement in the likelihood function and the 2D $\chi^2$. We find that no improvement is obtained with $n > 7$. Taking $n = 7$ the model requires 19 free parameters. Using a modified expression of Eq. (20) we obtain the fractions given in Table V. We observe a reduction of the $\rho(1450)\pi$ contribution by more than a factor of 10 compared to the results from the isobar model. However the $\rho(2150)\pi$ amplitude has a much larger contribution. We also observe a better fit quality as compared with the isobar model. The projection of the fit on the $\pi\pi$ mass in the $|\cos\theta_\pi| < 0.2$ region is shown in Fig. 7(c).

We note that the isobar model gives a better description of the $\rho(1450)$ region, while the Veneziano model describes better the high mass region. This may indicate that other resonances, apart from the low mass $\rho$ resonances, are contributing to the $J/\psi$ decay.
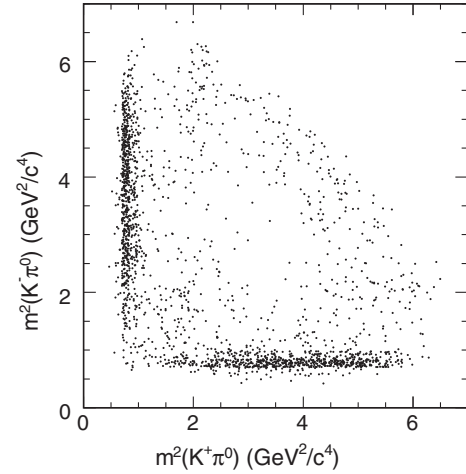


FIG. 10. Dalitz plot for the $J/\psi \to K^+ K^- \pi^0$ events in the signal region.

## B. Dalitz plot analysis of $J/\psi \to K^+ K^- \pi^0$

We perform a Dalitz plot analysis of $J/\psi \to K^+ K^- \pi^0$ in the $J/\psi$ signal region, defined in Table I, which contains 2102 events with $(88.8 \pm 0.7)\%$ purity, as determined from the fit shown in Fig. 3(b). Figure 10 shows the Dalitz plot for the $J/\psi$ signal region and Fig. 11 shows the Dalitz plot
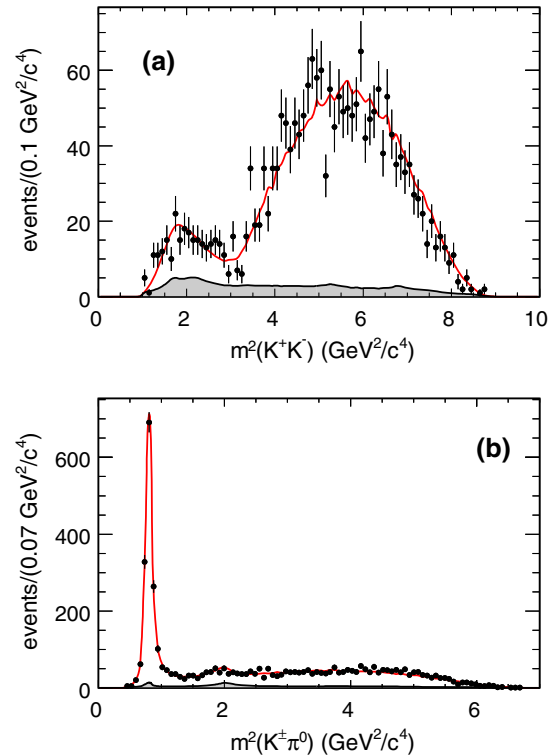


FIG. 11. The $J/\psi \to K^+ K^- \pi^0$ Dalitz plot projections. The superimposed curves result from the Dalitz plot analysis described in the text. The shaded regions show the background estimates obtained by interpolating the results of the Dalitz plot analyses of the sideband regions.

TABLE VI.   Results from the Dalitz plot analysis of the $J/\psi \to K^+K^-\pi^0$ signal region. When two uncertainties are given, the first is statistical and the second systematic.

| Final state | Fraction (%) | Phase (radians) |
|---|---|---|
| $K^*(892)^\pm K^\mp$ | $92.4 \pm 1.5 \pm 3.4$ | 0.0 |
| $\rho(1450)^0\pi^0$ | $9.3 \pm 2.0 \pm 0.6$ | $3.78 \pm 0.28 \pm 0.08$ |
| $K^*(1410)^\pm K^\mp$ | $2.3 \pm 1.1 \pm 0.7$ | $3.29 \pm 0.26 \pm 0.39$ |
| $K_2^*(1430)^\pm K^\mp$ | $3.5 \pm 1.3 \pm 0.9$ | $-2.32 \pm 0.22 \pm 0.05$ |
| Total | $107.4 \pm 2.8$ | |
| $\chi^2/\nu$ | $132/137 = 0.96$ | |

projections. We observe that the decay is dominated by the $K^*(892)^\pm K^\mp$ amplitude. We also observe a diagonal band which we tentatively attribute to the $\rho(1450)^0\pi^0$ amplitude.

As in the previous section, we fit the $J/\psi$ sideband regions to determine the background distribution. Due to the limited statistics and the low background, we take enlarged sidebands, defined as the ranges 2.910–3.005 GeV/$c^2$ and 3.176–3.271 GeV/$c^2$, respectively. Also in this case we fit these sidebands using noninterfering amplitudes described by relativistic Breit-Wigner functions using the method of the channel likelihood [23]. The $K^*\bar{K}$ contributions are symmetrized with respect to the kaon charge. Sideband regions are dominated by the presence of $K^*(892)\bar{K}$ and $K_2^*(1430)\bar{K}$ amplitudes.

We fit the $J/\psi \to K^+K^-\pi^0$ Dalitz plot using the isobar model. Also in this case amplitudes are added one at a time to ascertain the associated increase of the likelihood value and decrease of the 2D $\chi^2$ computed on the

$(m(K^+K^-), \cos\theta_h)$ plane. The results from the best fit are summarized in Table VI. We observe the following features:

(i) The decay is dominated by the $K^*(892)^\pm K^\mp$ and $\rho(1450)^0\pi^0$ amplitudes with smaller contributions from the $K_2^*(1430)^\pm K^\mp$ and $K_1^*(1410)^\pm K^\mp$ amplitudes.

(ii) We fix the $\rho(1450)$ and $\rho(1700)$ mass and width parameters to the values obtained from the $J/\psi \to \pi^+\pi^-\pi^0$ Dalitz plot analysis. This improves the description of the data, in comparison with a fit where the masses and widths are fixed to the PDG values [13].

(iii) $K^*(1680)K$, $\rho(1700)$, $\rho(2100)$, and NR have been tried but do not give significant contributions.

We therefore assign the broad enhancement in the $K^+K^-$ mass spectrum to the presence of the $\rho(1450)$ resonance: the present data do not require the presence of an exotic contribution. In evaluating the fractions we compute systematic uncertainties in a similar way as for the analysis of the $J/\psi \to \pi^+\pi^-\pi^0$ final state.

We compute the uncorrected Legendre polynomial moments $\langle Y_L^0 \rangle$ in each $K^+K^-$ and $K^\pm\pi^0$ mass interval by weighting each event by the relevant $Y_L^0(\cos\theta)$ function. These distributions are shown in Figs. 12 and 13. We also compute the expected Legendre polynomial moments from the weighted MC events and compare these with the experimental distributions. We observe good agreement for all the distributions, which indicates that the fit is able to reproduce the local structures apparent in the Dalitz plot.
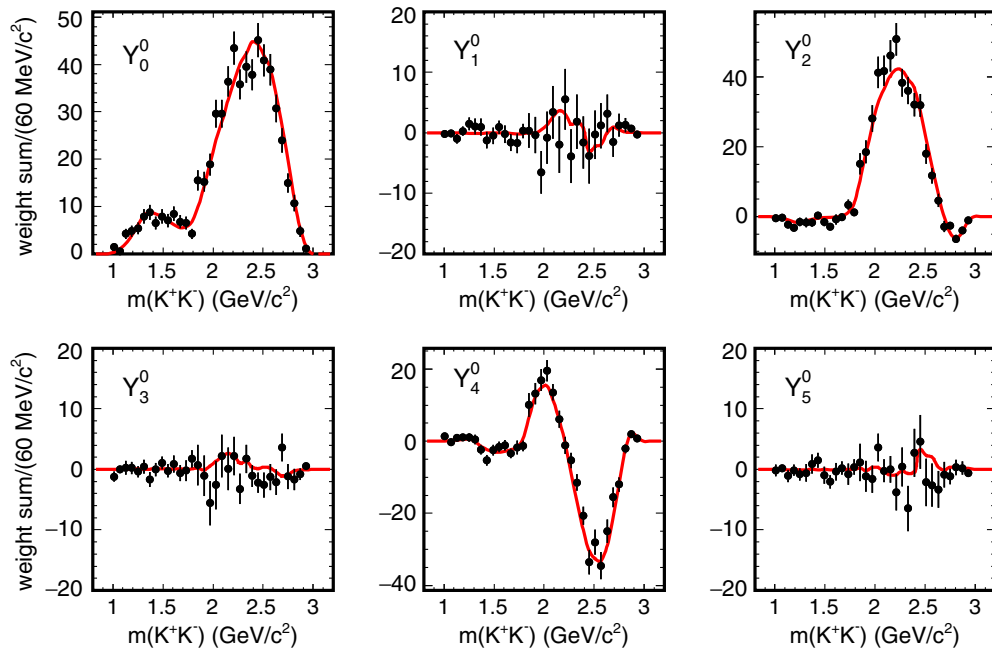


FIG. 12.   Legendre polynomial moments for $J/\psi \to K^+K^-\pi^0$ as a function of $K^+K^-$ mass. The superimposed curves result from the Dalitz plot analysis described in the text.
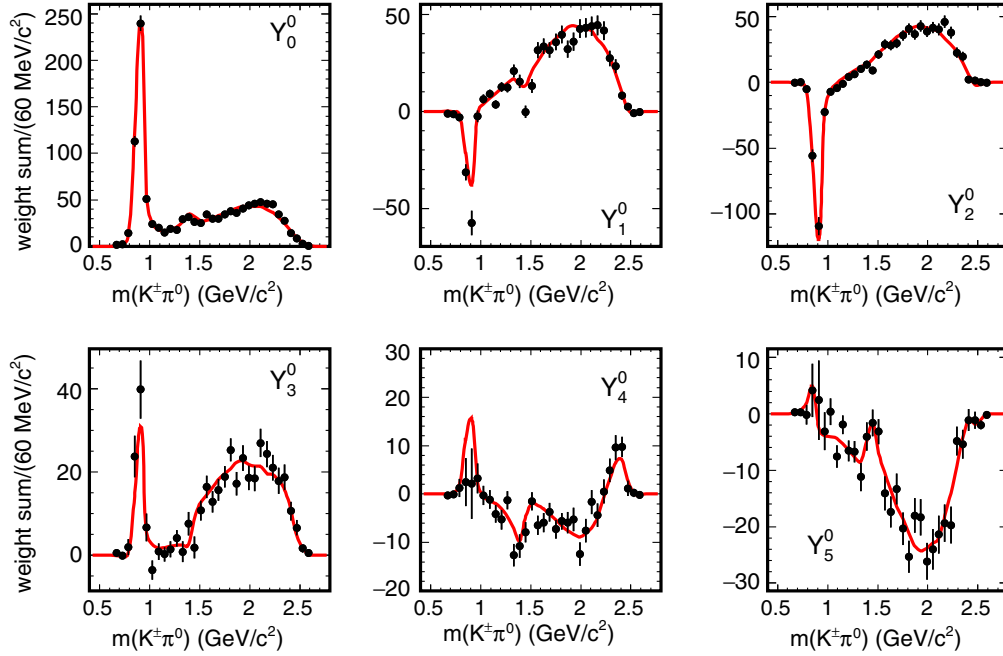
FIG. 13. Legendre polynomial moments for $J/\psi \to K^+ K^- \pi^0$ as a function of $K^\pm \pi^0$ mass. The superimposed curves result from the Dalitz plot analysis described in the text. The corresponding $K^+ \pi^0$ and $K^- \pi^0$ distributions are combined.

### C. Dalitz plot analysis of $J/\psi \to K_S^0 K^\pm \pi^\mp$

We perform a Dalitz plot analysis of $J/\psi \to K_S^0 K^\pm \pi^\mp$ in the $J/\psi$ signal region defined in Table I. This region contains 3907 events with $(93.1 \pm 0.4)\%$ purity, as determined from the fit shown in Fig. 3(c). Figure 14 shows the Dalitz plot for the $J/\psi$ signal region and Fig. 15 shows the Dalitz plot projections.

As in the previous sections, we fit the $J/\psi$ sideband regions to determine the background distribution using the channel likelihood [23] method.

We fit the $J/\psi \to K_S^0 K^\pm \pi^\mp$ Dalitz plot using the isobar model. Amplitudes have been included one by one testing the likelihood values and the 2D $\chi^2$ computed on the $(m(K_S^0 K^\pm), \cos \theta_h)$ plane. The results from the best fit are summarized in Table VII. We observe the following features:

(i) The decay is dominated by the $K^*(892)\bar{K}$, $K_2^*(1430)\bar{K}$, and $\rho(1450)^\pm \pi^\mp$ amplitudes with a smaller contribution from the $K_1^*(1410)\bar{K}$ amplitude.

(ii) We obtain a significant improvement of the description of the data by leaving free the $K^*(892)$ mass and width parameters and obtain

$$m(K^*(892)^+) = 895.6 \pm 0.8 \text{ MeV}/c^2,$$
$$\Gamma(K^*(892)^+) = 43.6 \pm 1.3 \text{ MeV},$$
$$m(K^*(892)^0) = 898.1 \pm 1.0 \text{ MeV}/c^2,$$
$$\Gamma(K^*(892)^0) = 52.6 \pm 1.7 \text{ MeV}. \quad (25)$$

The measured parameters for the charged $K^*(892)^+$ are in good agreement with those measured in $\tau$ lepton decays [13].

(iii) We fix the $\rho(1450)$ and $\rho(1700)$ parameters to the values obtained from the $J/\psi \to \pi^+ \pi^- \pi^0$ Dalitz plot analysis. This improves the description of the data in comparison with a fit where the masses and widths are fixed to the PDG values [13].

(iv) $K^*(1680)\bar{K}$, $\rho(1700)\pi$, $\rho(2100)\pi$, and NR amplitudes have been tried but do not give significant contributions.
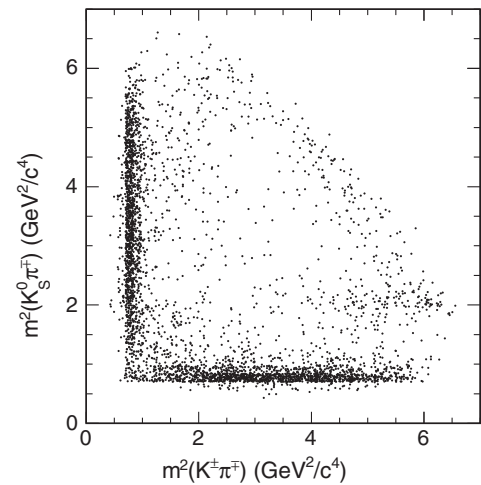


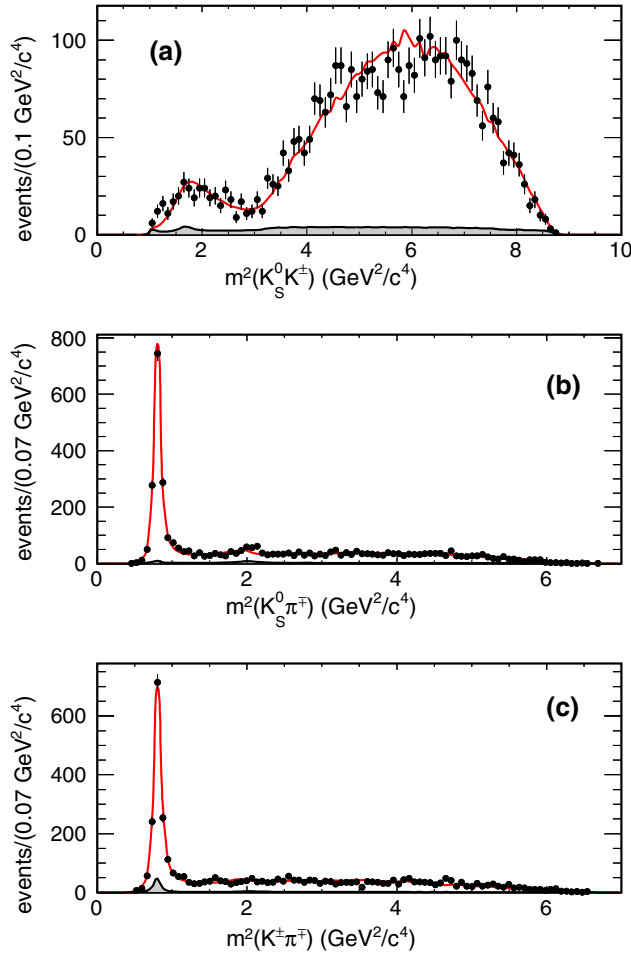FIG. 14. Dalitz plot for the $J/\psi \to K_S^0 K^\pm \pi^\mp$ events in the signal region.

FIG. 15. The $J/\psi \to K_S^0 K^\pm \pi^\mp$ Dalitz plot projections. The superimposed curves result from the Dalitz plot analysis described in the text. The shaded regions show the background estimates obtained by interpolating the results of the Dalitz plot analyses of the sideband regions.

We therefore assign the broad enhancement in the $K_S^0 K^\pm$ mass spectrum to the presence of the $\rho(1450)^\pm$ resonance. In evaluating the fractions we compute systematic uncertainties in a similar way as for the analysis of the

TABLE VII. Results from the Dalitz plot analysis of the $J/\psi \to K_S^0 K^\pm \pi^\mp$ signal region. When two uncertainties are given, the first is statistical and the second systematic.

| Final state | Fraction (%) | Phase (radians) |
|---|---|---|
| $K^*(892)\bar{K}$ | $90.5 \pm 0.9 \pm 3.8$ | $0.0$ |
| $\rho(1450)^\pm \pi^\mp$ | $6.3 \pm 0.8 \pm 0.6$ | $-3.25 \pm 0.13 \pm 0.21$ |
| $K_1^*(1410)\bar{K}$ | $1.5 \pm 0.5 \pm 0.9$ | $1.42 \pm 0.31 \pm 0.35$ |
| $K_2^*(1430)\bar{K}$ | $7.1 \pm 1.3 \pm 1.2$ | $-2.54 \pm 0.12 \pm 0.12$ |
| Total | $105.3 \pm 3.1$ | |
| $\chi^2/\nu$ | $274/217 = 1.26$ | |

$J/\psi \to \pi^+\pi^-\pi^0$ and $J/\psi \to K^+K^-\pi^0$ final states. We compute the uncorrected Legendre polynomial moments $\langle Y_L^0 \rangle$ in each $K_S^0 K^\pm$, $K^\pm \pi^\mp$, and $K_S^0 \pi^\mp$ mass interval by weighting each event by the relevant $Y_L^0(\cos\theta)$ function. These distributions are shown in Fig. 16 as functions of the $K_S^0 K^\pm$ mass and in Fig. 17 as functions of the $K\pi$ mass, combining the $K_S^0 \pi^\mp$ and $K^\pm \pi^\mp$ distributions. We also compute the expected Legendre polynomial moments from the weighted MC events and compare them with the experimental distributions. We observe good agreement for all the distributions, which indicates that the fit is able to reproduce the local structures apparent in the Dalitz plot.

## VII. MEASUREMENT OF THE $\rho(1450)^0$ RELATIVE BRANCHING FRACTION

In the Dalitz plot analysis of $J/\psi \to K^+K^-\pi^0$, the data are consistent with the observation of the decay $\rho(1450)^0 \to K^+K^-$. This allows a measurement of its relative branching fraction to $\rho(1450)^0 \to \pi^+\pi^-$.

We notice that the Veneziano model gives a $\rho(1450)$ contribution which is 10 times smaller than the isobar model. No equivalent Veneziano analysis of the $J/\psi \to K^+K^-\pi^0$ decay has been performed, therefore we perform a measurement of the $\rho(1450)$ relative branching fraction using the isobar model only.

We have measured in Sec. V [Eq. (11)] the ratio $\mathcal{R} = \mathcal{B}(J/\psi \to K^+K^-\pi^0)/\mathcal{B}(J/\psi \to \pi^+\pi^-\pi^0)$ and obtain $\mathcal{R} = 0.120 \pm 0.003 \pm 0.009$. From the Dalitz plot analysis of $J/\psi \to \pi^+\pi^-\pi^0$ and $J/\psi \to K^+K^-\pi^0$ we obtain the $\rho(1450)^0$ fractions whose systematic uncertainties are found to be independent. From the Dalitz plot analysis of $J/\psi \to \pi^+\pi^-\pi^0$ we obtain

$$
\begin{aligned}
\mathcal{B}_1 &= \frac{\mathcal{B}(J/\psi \to \rho(1450)^0 \pi^0)\mathcal{B}(\rho(1450)^0 \to \pi^+\pi^-)}{\mathcal{B}(J/\psi \to \pi^+\pi^-\pi^0)} \\
&= [(10.9 \pm 1.7(\text{stat}) \pm 2.7(\text{sys}))/3.]\% \\
&= (3.6 \pm 0.6(\text{stat}) \pm 0.9(\text{sys}))\%.
\end{aligned}
\tag{26}
$$

From the Dalitz plot analysis of $J/\psi \to K^+K^-\pi^0$ we obtain

$$
\begin{aligned}
\mathcal{B}_2 &= \frac{\mathcal{B}(J/\psi \to \rho(1450)^0 \pi^0)\mathcal{B}(\rho(1450)^0 \to K^+K^-)}{\mathcal{B}(J/\psi \to K^+K^-\pi^0)} \\
&= (9.3 \pm 2.0(\text{stat}) \pm 0.6(\text{sys}))\%.
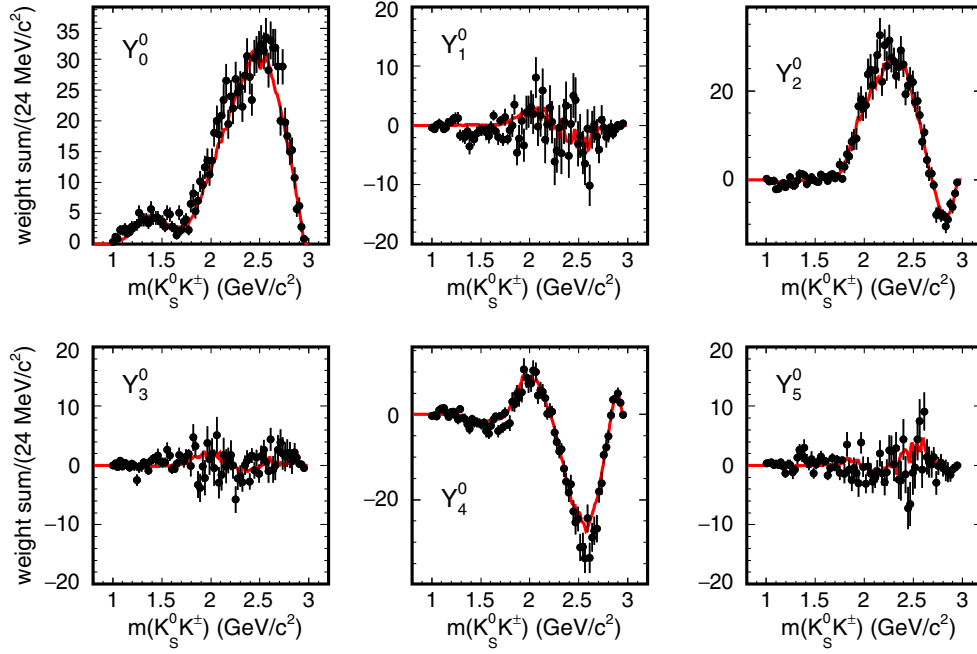\end{aligned}
\tag{27}
$$

We therefore obtain

FIG. 16. Legendre polynomial moments for $J/\psi \to K_S^0 K^{\pm} \pi^{\mp}$ as a function of $K_S^0 K^{\pm}$ mass. The superimposed curves result from the Dalitz plot analysis described in the text.
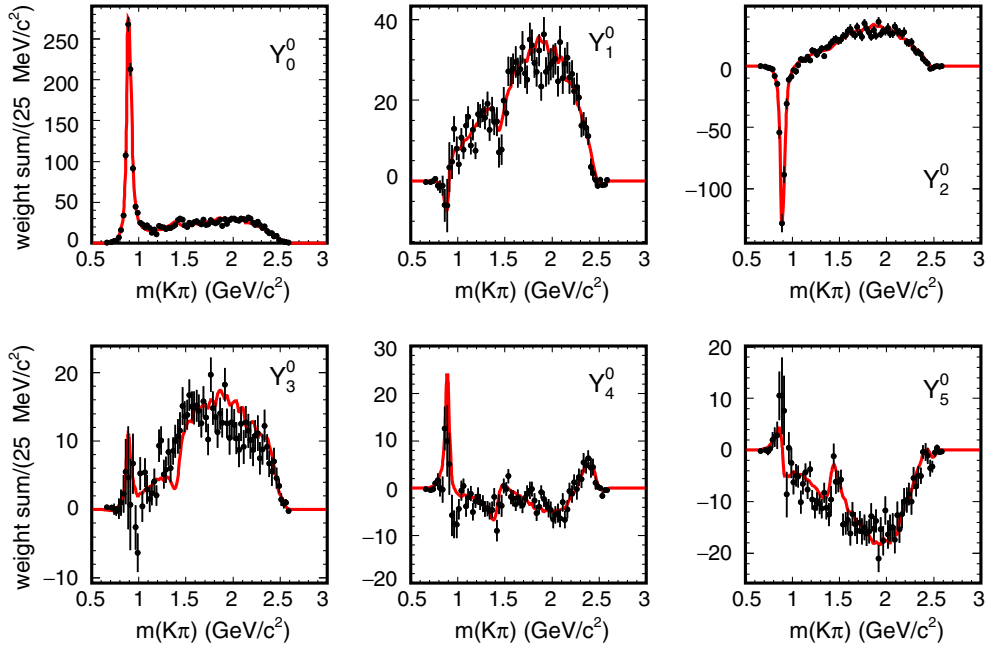


FIG. 17. Legendre polynomial moments for $J/\psi \to K_S^0 K^{\pm} \pi^{\mp}$ as a function of $K\pi$ mass. The superimposed curves result from the Dalitz plot analysis described in the text. The corresponding $K_S^0 \pi^{\mp}$ and $K^{\pm} \pi^{\mp}$ distributions are combined.

$$\frac{\mathcal{B}(\rho(1450)^0 \to K^+ K^-)}{\mathcal{B}(\rho(1450)^0 \to \pi^+ \pi^-)} = \frac{\mathcal{B}_2}{\mathcal{B}_1} \cdot \mathcal{R}$$

$$= 0.307 \pm 0.084(\text{stat}) \pm 0.082(\text{sys}). \qquad (28)$$

## VIII. SUMMARY

We study the processes $e^+ e^- \to \gamma_{\text{ISR}} J/\psi$ where $J/\psi \to \pi^+ \pi^- \pi^0$, $J/\psi \to K^+ K^- \pi^0$, and $J/\psi \to K_S^0 K^{\pm} \pi^{\mp}$ using a data sample of 519 fb$^{-1}$ recorded with the *BABAR* detector operating at the SLAC PEP-II asymmetric-energy $e^+ e^-$

collider at center-of-mass energies at and near the $\Upsilon(nS)$ ($n=2,3,4$) resonances. We measure the branching fractions:
$\mathcal{R}_1 = \frac{\mathcal{B}(J/\psi \to K^+K^-\pi^0)}{\mathcal{B}(J/\psi \to \pi^+\pi^-\pi^0)} = 0.120 \pm 0.003(\text{stat}) \pm 0.009(\text{sys})$, and
$\mathcal{R}_2 = \frac{\mathcal{B}(J/\psi \to K_S^0 K^\pm \pi^\mp)}{\mathcal{B}(J/\psi \to \pi^+\pi^-\pi^0)} = 0.265 \pm 0.005(\text{stat}) \pm 0.021(\text{sys})$. We perform Dalitz plot analyses of the three $J/\psi$ decay modes and measure fractions for resonances contributing to the decays. We also perform a Dalitz plot analysis of $J/\psi \to \pi^+\pi^-\pi^0$ using the Veneziano model. We observe structures compatible with the presence of $\rho(1450)^0$ in both $J/\psi \to \pi^+\pi^-\pi^0$ and $J/\psi \to K^+K^-\pi^0$ and measure the ratio of branching fractions: $\mathcal{R}(\rho(1450)^0) = \frac{\mathcal{B}(\rho(1450)^0 \to K^+K^-)}{\mathcal{B}(\rho(1450)^0 \to \pi^+\pi^-)} = 0.307 \pm 0.084(\text{stat}) \pm 0.082(\text{sys})$.

# ACKNOWLEDGMENTS

## APPENDIX: INTERFERENCE FIT FRACTIONS AND VENEZIANO MODEL COEFFICIENTS

The central values and statistical errors for the interference fit fractions are shown in Tables VIII, IX, and X, for the $J/\psi \to \pi^+\pi^-\pi^0$, $J/\psi \to K^+K^-\pi^0$, and $J/\psi \to K_S^0 K^\pm \pi^\mp$, respectively. Table XI reports the fitted $c_{X \to abc}(n,m)$ coefficients with statistical uncertainties from the Veneziano model description of $J/\psi \to \pi^+\pi^-\pi^0$.

TABLE VIII. Interference fit fractions (%) and statistical uncertainties from the Dalitz plot analysis of $J/\psi \to \pi^+\pi^-\pi^0$. The amplitudes are: $(A_0)\,\rho(770)\pi$, $(A_1)\,\rho(1450)\pi$, $(A_2)\,\rho(1700)\pi$, $(A_3)\,\rho(2150)\pi$, $(A_4)\,\omega(783)\pi^0$. The diagonal elements are the same as the conventional fit fractions.

|       | $A_0$ | $A_1$ | $A_2$ | $A_3$ | $A_4$ |
|-------|-------|-------|-------|-------|-------|
| $A_0$ | $114.2\pm1.1$ | $-10.4\pm0.8$ | $0.7\pm0.1$ | $0.1\pm0.1$ | $-1.1\pm0.3$ |
| $A_1$ | | $10.9\pm1.7$ | $-1.7\pm0.6$ | $-0.2\pm0.1$ | $0.0\pm0.0$ |
| $A_2$ | | | $0.8\pm0.2$ | $-0.07\pm0.02$ | $0.0\pm0.0$ |
| $A_3$ | | | | $0.04\pm0.01$ | $0.0\pm0.0$ |
| $A_4$ | | | | | $0.08\pm0.03$ |

TABLE IX. Interference fit fractions (%) and statistical uncertainties from the Dalitz plot analysis of $J/\psi \to K^+K^-\pi^0$. The amplitudes are: $(A_0)\,K^*(892)^\pm K^\mp$, $(A_1)\,\rho(1450)^0\pi^0$, $(A_2)\,K^*(1410)^\pm K^\mp$, $(A_3)\,K_2^*(1430)^\pm K^\mp$. The diagonal elements are the same as the conventional fit fractions.

|       | $A_0$ | $A_1$ | $A_2$ | $A_3$ |
|-------|-------|-------|-------|-------|
| $A_0$ | $92.4 \pm 1.5$ | $-5.5 \pm 0.6$ | $-0.7 \pm 0.1$ | $-0.9 \pm 0.2$ |
| $A_1$ | | $9.3 \pm 2.0$ | $2.2 \pm 0.7$ | $2.1 \pm 0.4$ |
| $A_2$ | | | $2.3 \pm 1.1$ | $3.3 \pm 0.9$ |
| $A_3$ | | | | $3.5 \pm 1.3$ |

TABLE X. Interference fit fractions (%) and statistical uncertainties from the Dalitz plot analysis of $J/\psi \to K_S^0 K^\pm \pi^\mp$. The amplitudes are: $(A_0)\,K^*(892)\bar{K}$, $(A_1)\,\rho(1450)^\pm\pi^\mp$, $(A_2)\,K_1^*(1410)\bar{K}$, $(A_3)\,K_2^*(1430)\bar{K}$. The diagonal elements are the same as the conventional fit fractions.

|       | $A_0$ | $A_1$ | $A_2$ | $A_3$ |
|-------|-------|-------|-------|-------|
| $A_0$ | $90.5 \pm 0.9$ | $-5.4 \pm 0.4$ | $0.1 \pm 0.1$ | $-1.3 \pm 0.2$ |
| $A_1$ | | $6.3 \pm 0.8$ | $-0.1 \pm 0.5$ | $1.9 \pm 0.3$ |
| $A_2$ | | | $1.5 \pm 0.5$ | $3.3 \pm 1.6$ |
| $A_3$ | | | | $7.1 \pm 1.3$ |

TABLE XI. Fitted $c_{X \to abc}(n,m)$ coefficients with statistical uncertainties from the Veneziano model description of $J/\psi \to \pi^+\pi^-\pi^0$.

| $n$ | $m$ | $c_{X \to abc}(n,m)$ |
|-----|-----|----------------------|
| 1 | 1 | $0.5720 \pm 0.0016$ |
| 2 | 1 | $0.7380 \pm 0.0027$ |
| 3 | 1 | $0.1165 \pm 0.0014$ |
|   | 2 | $4901 \pm 426$ |
| 4 | 1 | $354 \pm 53$ |
|   | 2 | $1781 \pm 49$ |
| 5 | 1 | $-137.4 \pm 3.4$ |
|   | 2 | $2087 \pm 245$ |
|   | 3 | $-248 \pm 25$ |
| 6 | 1 | $1869 \pm 86$ |
|   | 2 | $-354 \pm 10$ |
|   | 3 | $9.8 \pm 0.3$ |
| 7 | 1 | $1084 \pm 132$ |
|   | 2 | $63.5 \pm 13.7$ |
|   | 3 | $-1.0 \pm 0.4$ |
|   | 4 | $6259 \pm 335$ |

[1] L. Kopke and N. Wermes, Phys. Rep. **174**, 67 (1989).

[2] J. Z. Bai *et al.* (BES Collaboration), Phys. Rev. D **68**, 052003 (2003).

[3] V. Mathieu, N. Kochelev, and V. Vento, Int. J. Mod. Phys. E **18**, 1 (2009).

[4] J. Z. Bai *et al.* (BESII Collaboration), Phys. Rev. D **70**, 012005 (2004).

[5] M. Ablikim *et al.* (BESIII Collaboration), Phys. Lett. B **710**, 594 (2012).

[6] P. Guo, R. Mitchell, and A. P. Szczepaniak, Phys. Rev. D **82**, 094002 (2010).

[7] A. P. Szczepaniak and M. R. Pennington, Phys. Lett. B **737**, 283 (2014).

[8] M. E. B. Franklin *et al.* (Mark II Collaboration), Phys. Rev. Lett. **51**, 963 (1983).

[9] L. P. Chen and W. Dunwoodie (Mark III Collaboration), Report No. SLAC-PUB-5674, 1991.

[10] M Ablikim *et al.* (BESII Collaboration), Phys. Rev. Lett. **97**, 142002 (2006).

[11] B. A. Li, Phys. Rev. D **76**, 094016 (2007).

[12] X. Liu, B. Zhang, L.-L. Shen, and S.-L. Zhu, Phys. Rev. D **75**, 074017 (2007).

[13] C. Patrignani *et al.* (Particle Data Group), Chin. Phys. C **40**, 100001 (2016).

[14] J. P. Lees *et al.* (*BABAR* Collaboration), Nucl. Instrum. Methods Phys. Res., Sect. A **726**, 203 (2013).

[15] B. Aubert *et al.* (*BABAR* Collaboration), Nucl. Instrum. Methods Phys. Res., Sect. A **479**, 1 (2002); **729**, 615 (2013).

[16] The *BABAR* detector Monte Carlo simulation is based on GEANT4 [S. Agostinelli *et al.*, Nucl. Instrum. Methods Phys. Res., Sect. A **506**, 250 (2003)] and EVTGEN [D. J. Lange, Nucl. Instrum. Methods Phys. Res., Sect. A **462**, 152 (2001)].

[17] B. Aubert *et al.* (*BABAR* Collaboration), Phys. Rev. D **79**, 112001 (2009).

[18] M. J. Oreglia, Ph.D. thesis, Stanford University, 1980; J. E. Gaiser, Ph.D. thesis, Stanford University, 1982; T. Skwarnicki, Ph.D. thesis, Institut of Nuclear Physics, Cracow 1986.

[19] F. Vannucci *et al.* (Mark I Collaboration), Phys. Rev. D **15**, 1814 (1977).

[20] C. Zemach, Phys. Rev. **133**, B1201 (1964).

[21] C. Dionisi *et al.*, Nucl. Phys. **B169**, 1 (1980).

[22] P. Colangelo (private communication).

[23] P. E. Condon and P. L. Cowell, Phys. Rev. D **9**, 2558 (1974).

[24] J. Blatt and V. Weisskopf, *Theoretical Nuclear Physics* (John Wiley & Sons, New York, 1952).